FRIEDREICH'S ATAXIA

Treatment with ROS detoxifying gold quantum clusters alleviates the functional decline in a mouse model of Friedreich ataxia

Chiara Villa[1], Mariella Legato[1], Alessandro Umbach[2], Chiara Riganti[3], Rebecca Jones[2], Beatrice Martini[1], Marina Boido[4], Claudio Medana[2], Irene Facchinetti[5], Dario Barni[5], Milena Pinto[6], Tania Arguello[6], Marzia Belicchi[1], Gigliola Fagiolari[7], Carla Liaci[2], Maurizio Moggio[7], Riccardo Ruffo[5], Carlos T. Moraes[6], Angelo Monguzzi[5], Giorgio R. Merlo[2], Yvan Torrente[1]*

Friedreich ataxia (FRDA) is caused by the reduced expression of the mitochondrial protein frataxin (FXN) due to an intronic GAA trinucleotide repeat expansion in the *FXN* gene. Although FRDA has no cure and few treatment options, there is research dedicated to finding an agent that can curb disease progression and address symptoms as neurobehavioral deficits, muscle endurance, and heart contractile dysfunctions. Because oxidative stress and mitochondrial dysfunctions are implicated in FRDA, we demonstrated the systemic delivery of catalysts activity of gold cluster superstructures (Au_8-pXs) to improve cell response to mitochondrial reactive oxygen species and thereby alleviate FRDA-related pathology in mesenchymal stem cells from patients with FRDA. We also found that systemic injection of Au_8-pXs ameliorated motor function and cardiac contractility of YG8sR mouse model that recapitulates the FRDA phenotype. These effects were associated to long-term improvement of mitochondrial functions and antioxidant cell responses. We related these events to an increased expression of frataxin, which was sustained by reduced autophagy. Overall, these results encourage further optimization of Au_8-pXs in experimental clinical strategies for the treatment of FRDA.

INTRODUCTION

Friedreich ataxia (FRDA) is a multisystemic autosomal recessive disorder caused by a GAA repeat expansion mutation within intron 1 of the FXN gene (*1*) that determines reduced expression of the mitochondrial protein FXN (*2*). Frataxin dysregulation is linked to dysfunctions of the mitochondrial energy conversion and oxidative phosphorylation (OXPHOS) through iron accumulation and increased production of reactive oxygen species (ROS), leading to oxidative stress especially in mitochondria (*3*). Cellular antioxidant response is regulated by nuclear factor E2–related factor 2 (Nrf2) transcription factor that induces the expression of ROS-response antioxidant genes, by binding to the antioxidant response element (ARE) on nuclear DNA, including an ARE site within the FXN gene (*4*). In patients with FRDA and mouse models, Nrf2 is compromised in response to oxidative insults, thus leading to reduced expression of antioxidant genes such as superoxide dismutase (SOD) SOD1 and SOD2 (*5*). In addition, frataxin deficiency is associated with the down-regulation of PGC-1α [peroxisome proliferator–activated receptor γ (PPARγ) coactivator 1α], a regulator of mitochondrial biogenesis (*6*), suggesting an early impairment of mitochondrial pathways (*7*). Another hallmark of FRDA is the formation of giant or larger disorganized mitochondria in rodent muscles (*8*) or in cultured cells (*9*) triggered by increased expression of the mitochondrial fusion protein mitofusin 1 (Mfn1). Because metabolic stress triggers salvaging processes, by which macromolecules and organelles are targeted by autophagic vesicles to lysosomes for degradation and recycling of their constituents, autophagy may be considered a key node for the regulation of ROS amount and ROS-dependent pathway (*10*).

It is likely that alterations in ROS and imbalance of mitochondrial dynamics and autophagy are critically implicated in FRDA pathology (*9*), and they represent a common pathogenic element to several neurodegenerative diseases such as Parkinson's disease, Charcot-Marie-Tooth disease, Alzheimer's disease, Huntington's disease, or amyotrophic lateral sclerosis (*11*). Pathologically, frataxin insufficiency leads to spinocerebellar neurodegeneration, ataxia, muscle weakness, cardiomyopathy, diabetes mellitus, and skeletal deformities (*12*). No cure or effective treatment has been reported for FRDA. Emerging therapies are directed at the augmentation of mitochondrial function (such as antioxidants, Nrf2 up-regulators, and deuterated fatty acids) and frataxin restoration [such as gene and cell therapy, erythropoietin, interferon-γ, nicotinamide, and histone deacetylase inhibitor (HDACi)] (*13*–*15*). Buffering the abundance of ROS and the oxidative stress–induced damages in FRDA was the initial challenge of exploiting gold quantum clusters [Au_8 gold cluster superstructures (Au_8-pXs)] as potential therapeutic strategy for FRDA. Au_8-pX is a recently developed highly biocompatible material based on gold quantum clusters, subnanometer structures made from few units to hundred gold atoms, which have excellent ROS scavenger potential (*16*, *17*), probably related to their catalytic activity (*18*). In our study, we examined the effects of Au_8-pX treatment on bone marrow–derived

[1]Stem Cell Laboratory, Department of Pathophysiology and Transplantation, Università degli Studi di Milano, Fondazione IRCCS Ca' Granda Ospedale Maggiore Policlinico, Centro Dino Ferrari, Via F. Sforza 35, 20122 Milano, Italy. [2]Department of Molecular Biotechnology and Health Science, University of Turin, Via Nizza, 52 10126 Torino, Italy. [3]Department of Oncology, University of Turin, Via Santena 5/bis, 10126 Torino, Italy. [4]Department of Neuroscience "Rita Levi Montalcini", Neuroscience Institute Cavalieri Ottolenghi, University of Turin, Regione Gonzole 10, Orbassano,10043 Torino, Italy. [5]Department of Material Science, University of Milano Bicocca, Via R. Cozzi 55, 20125 Milano, Italy. [6]Department of Neurology, University of Miami Miller School of Medicine, Miami, FL 33136, USA. [7]Neuromuscular and Rare Diseases Unit, Fondazione IRCCS Ca'Granda Ospedale Maggiore Policlinico, Via F. Sforza 35, 20122 Milan, Italy.
*Corresponding author. Email: yvan.torrente@unimi.it

mesenchymal stem cells (BMSCs) from patients with FRDA, and, serendipitously, we found that Au_8-pXs not only acted as an antioxidant to relieve the oxidative stress improving the mitochondrial function but also rescued the autophagy flux and increased FXN protein expression, which would be the fundamental resolution for patients with FRDA.

Moreover, the intravenous delivery of Au_8-pXs into the YG8sR mouse model, which resembles the FRDA progressive neurological degeneration and muscle weakness (*19*), rescued many aspects of the ataxic phenotype including neuromotor and cardiac deficits, and mitochondrial response to oxidative stress. Treatment with Au_8-pXs may represent an effective strategy for treating FRDA therapy.

RESULTS

ROS buffering effect of Au_8-pXs

We recently demonstrated that Au_8-pXs have anticytotoxic and ROS-scavenging ability (*16*), which could be linked to the catalytic effect of Au nanostructures on chemical and photochemical reactions involving oxygen (*18*). We therefore investigated the possible ROS-specific interactions of Au_8-pXs to point out a preferential pathway for their therapeutic effect on FRDA. Au_8-pX ultraviolet-visible (UV/Vis) absorption and the photoluminescence profile in aqueous dispersion peaked at 380 and 520 nm, respectively (fig. S1A). The interaction of Au_8-pXs with singlet oxygen ($^1O_2$*), superoxide ($O_2^{\bullet-}$), and hydrogen peroxide (H_2O_2) was investigated by titration experiments in water solution using ROS-specific sensitization methods. The relative concentration of ROS was monitored as a function of time by means of continuous wave (cw) optical probing techniques. For singlet oxygen, we used the fluorescent compound Singlet Oxygen Sensore Green (SOSG) whose photoluminescence intensity is proportional to the amount of singlet oxygen (*20*). In the reference SOSG dispersion, the slight increment of +25% mirrored the spontaneous formation of singlet oxygen in the aqueous environment (fig. S1B). By adding Au_8-pXs, no variation was observed, suggesting the occurrence of an interaction that reduces ROS final concentration. In line, when singlet oxygen amount was artificially increased by Rose Bengal dye as photosensitizer (*21*), the singlet oxygen concentration increased up to +300% in the time span in the absence of Au_8-pXs, more than one order of magnitude than the reference value. Conversely, Au_8-pXs progressively reduced the singlet oxygen amount to photosensitizer-free sample concentration and further decreased to a final value of +12%, lower than in the reference sample.

Superoxide species were generated by exploiting the photolysis of H_2O_2 under cw UV excitation at 405 nm in the aqueous solution (*22*), and the superoxide amount was monitored by means of the probe MitoSOX red excited at 532 nm (fig. S1C). In the absence of gold cluster superstructures, the progressive addition and photolysis of H_2O_2 increased the superoxide concentration until it reached a saturation plateau that corresponded to an increment of the ROS relative concentration of +450%. Conversely, in the presence of Au_8-pXs, only a negligible variation of as large as +20% was observed, thus demonstrating an excellent scavenging of superoxide.

A less effective but still appreciable effect of Au_8-pXs was observed for the H_2O_2 species (fig. S1D). The relative concentration of H_2O_2 was monitored by the molecular optical probe diphenyl-1-pyrenylphosphine (*23*) upon progressive addition of H_2O_2 to a water solution. Despite the result that scavenging was not as large as in the previous cases, a reduction of the final H_2O_2 amount in the presence of Au_8-pXs by a factor 20% was detectable. We then demonstrated the Au_8-pX catalytic activity for ROS degradation by means of cyclic voltammetry experiments in phosphate-buffered saline (PBS):H_2O_2 solution, in the presence and absence of Au_8-pXs (fig. S1, E and F). Figure S1E reports the cyclic voltammetry of PBS on a Au electrode, in the potential range between −0.5 and 1.0 V versus saturated calomelan electrode, where PBS was completely unaffected by voltage and only small capacitive current was observed. When H_2O_2 was added, a Faradaic current appeared related to the redox processes of the oxygen peroxides. The oxidation peak intensity decreased with the number of cycles, in agreement with the progressive transformation of all the H_2O_2 in solution into water and oxygen molecules. In the presence of Au_8-pXs, the PBS:Au_8-pX mixture was again electrochemically inactive at any applied voltage, and no current variation was detectable in correspondence of H_2O_2 oxidation potential (fig. S1F). These results demonstrated the huge catalytic effect of the gold cluster superstructures for the oxidation reaction that immediately depurated the liquid environment from the ROS species hindering its electrochemical signature.

Au_8-pX–dependent modulation of the autophagy pathway increases mFXN expression

Frataxin down-regulation as in FRDA causes ROS overload, iron-sulfur (Fe-S) cluster proteins, impairment, and iron accumulation, leading to defects in the stability, integrity, and homeostasis of mitochondria (*11*, *24*). Considering the ROS scavenger ability of Au_8-pXs in menadione-stressed cell lines (*16*), we sought to document this therapeutic potential in mesenchymal stem cells isolated from two healthy donors ($BMSCs^{CTR\#1}$ and $BMSCs^{CTR\#2}$) and two age-matched patients with FRDA ($BMSCs^{FRDA\#1}$ and $BMSCs^{FRDA\#2}$). BMSCs expanded in vitro for three to five passages expressed the antigens CD90 (90.7%), CD73 (91.6%), CD105 (92.9%), and CD44 (91.3%) (fig. S2A). They did not display expression of hematopoietic surface antigens CD34 and CD45, thereby confirming the mesenchymal immunophenotype (fig. S2A) (*25*). The optimal concentration and loading time of Au_8-pXs for BMSC treatment was determined to be within the range of 5 to 10 μM for 24 hours, in line with our previous results (*16*) (Fig. 1). Confocal images of BMSCs confirmed the uptake of clusters, detectable by their own fluorescence emission at 405-nm laser excitation (fluorescence intensity per cell: 174.95 ± 46.04 for 5 μM Au_8-pX $BMSCs^{FRDA\#1}$; 208.006 ± 47.58 for 10 μM Au_8-pX $BMSCs^{FRDA\#1}$; 154.48 ± 20.90 for 5 μM Au_8-pX $BMSCs^{FRDA\#2}$; 190.29 ± 25.25 for 10 μM Au_8-pX $BMSCs^{FRDA\#2}$) (Fig. 1, A and B). When the Au_8-pX dose increases over 5 to 10 μM, the uptake augmented in $BMSCs^{FRDA\#1}$ and $BMSCs^{FRDA\#2}$, as confirmed by quantification of the fluorescence intensity signal ($P = 0.0091$ and $P = 0.0288$, respectively). Thanks to their reduced dimensions, and while lacking targeting features, Au_8-pXs partially enter mitochondria, as monitored by Mitotracker staining, indicating a widespread distribution within different cell compartments (Pearson correlation coefficient for MitoTracker and Au_8-pXs: 0.584 ± 0.072 for 5 μM Au_8-pX $BMSCs^{FRDA\#1}$; 0.717 ± 0.070 for 10 μM Au_8-pX $BMSCs^{FRDA\#1}$; 0.538 ± 0.084 for 5 μM Au_8-pX $BMSCs^{FRDA\#2}$; 0.614 ± 0.085 for 10 μM Au_8-pX $BMSCs^{FRDA\#2}$). $BMSCs^{FRDA}$ from both patients treated with 10 μM Au_8-pXs showed a higher colocalization with MitoTracker staining than 5 μM Au_8-pX–treated cells ($P < 0.0001$ for $BMSCs^{FRDA\#1}$; $P < 0.0134$ for $BMSCs^{FRDA\#2}$) (Fig. 1B).

We next examined the pathophysiological consequences of FXN deficiency in iron-sulfur (Fe-S) cluster biogenesis and mitochondrial

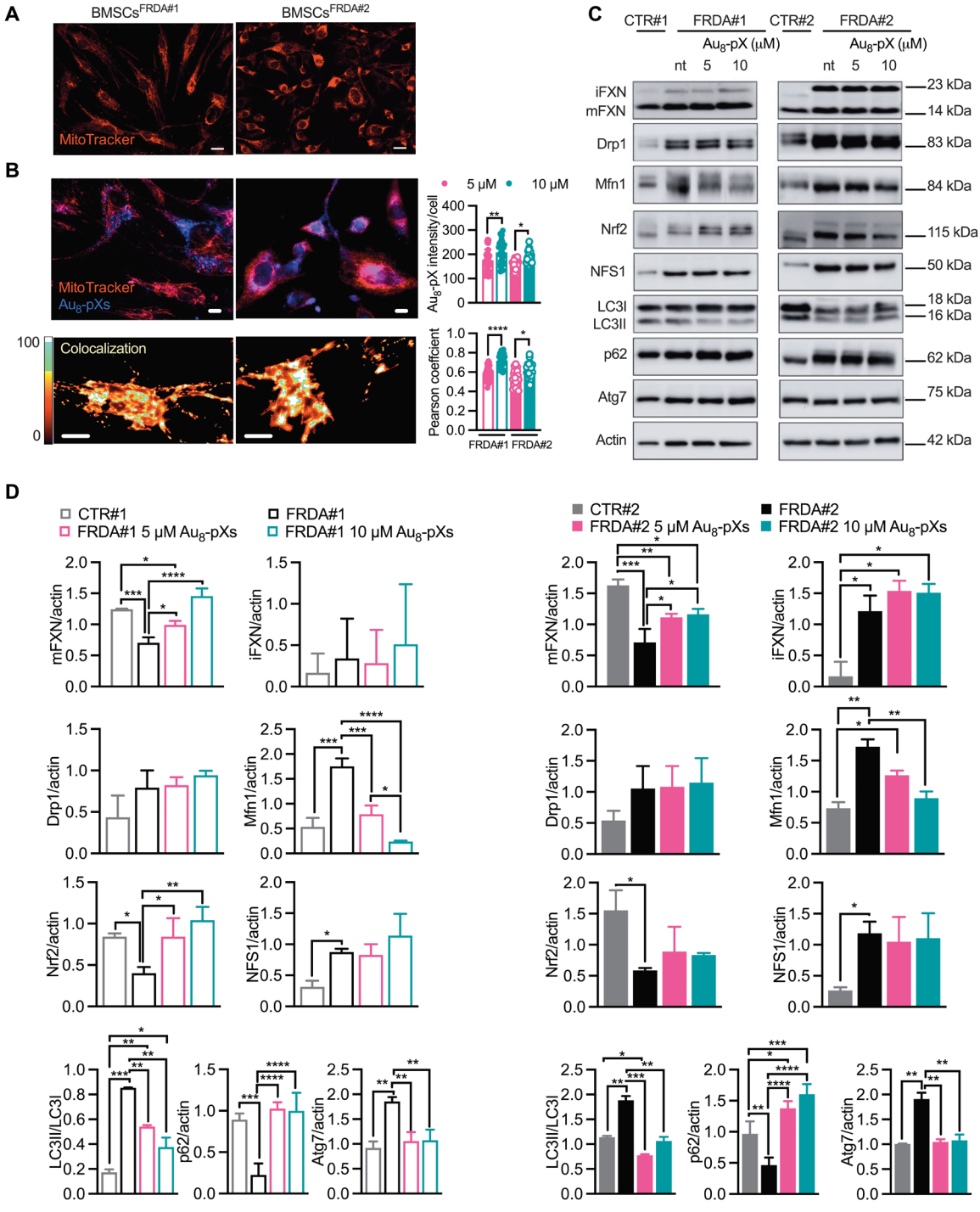

Fig. 1. Au_8-pX modulation of the autophagy pathway in FRDA-derived BMSCs. (**A**) Representative confocal images of mitochondria in BMSCs derived from patients with FRDA#1 ($BMSCs^{FRDA\#1}$) and FRDA#2 ($BMSCs^{FRDA\#2}$) stained with MitoTracker Red CMXRos ($n = 2$ to 4 cell plates per group). Scale bars, 25 μm. (**B**) Representative confocal images and quantification by ImageJ of BMSCs derived from patients with FRDA#1 and FRDA#2 labeled with 10 μM Au_8-pXs for 24 hours and stained with MitoTracker Red CMXRos. Au_8-pXs were excited with 405-nm UV/Vis, and emitted fluorescence was collected between 500 and 540 nm. Scale bars, 10 μm. Lower panel depicts heatmap images of colocalization (yellow) of mitochondrial staining and Au_8-pXs through EZColocalization plugin of ImageJ. Colocalization and segmentation were determined by Pearson correlation coefficient. Scale bars, 5 μm. Data were expressed as means ± SD ($n = 4$ to 6 fields per cell type, $n = 5$ wells). (**C**) Representative Western blots of frataxin (intermediate form iFXN and mature protein mFXN) and FXN-related proteins (Nrf2 and NFS1), mitochondrial fusion (Mfn1) and fission [dynamin-related protein 1 (Drp1)] proteins, and proteins related to the autophagic flux (LC3I, LC3II, p62, and Atg7) in Au_8-pX–treated and untreated (nt) $BMSCs^{FRDA}$. BMSCs from age-matched healthy donors (CTR#1 and CTR#2) were evaluated as controls. Actin was used as loading control. (**D**) Representative Western blot quantification of protein bands in Au_8-pX–treated and untreated (nt) $BMSCs^{FRDA}$ and age-matched $BMSCs^{CTR}$. Data were expressed as means ± SD ($n = 2$ to 4 independent experiments); $^*P < 0.05$, $^{**}P < 0.01$, $^{***}P < 0.001$, and $^{****}P < 0.0001$ [ordinary one-way analysis of variance (ANOVA), Bonferroni's test].

metabolism of BMSCs^{FRDA}. FXN functions as an allosteric activator of the sulfur donor enzyme NFS1 and as a modulator of iron entrance into a multiprotein Fe-S cluster assembling system (*26*). This latter in the presence of low FXN is unable to work at a proper rate, resulting in decreased iron sulfur cluster biogenesis and activity of respiratory chain complexes, especially I, II, and III. NFS1 overexpression was found in both BMSCs$^{FRDA\#1}$ ($P = 0.0314$) and BMSCs$^{FRDA\#2}$ ($P = 0.0157$) versus BMSCs^{CTR} (Fig. 1, C and D), without changes after Au_8-pX treatment (Fig. 1, C and D). FXN deficiency further hampers dynamic processes such as mitochondrial biogenesis, fusion/fission, mitophagy, and apoptosis (*27*). BMSCs$^{FRDA\#1}$ and BMSCs$^{FRDA\#2}$ showed increased expression of Mfn1 compared to the BMSCs$^{CTR\#1}$ ($P = 0.0002$) and BMSCs$^{CTR\#2}$ ($P = 0.0035$), suggesting prevalence of mitochondrial fusion over fission (Fig. 1, C and D), in agreement with previous reports that correlated a giant morphology to a dysfunctional mitochondrion in FRDA cell and animal models (*8*). We found that Au_8-pX administration at 10 μM was able to determine a substantial decrease of Mfn1 expression in treated BMSCs$^{FRDA\#1}$ ($P < 0.0001$) and BMSCs$^{FRDA\#2}$ ($P = 0.0071$), whereas 5 μM Au_8-pX dose induced a significantly reduction of Mfn1 only in treated BMSCs$^{FRDA\#1}$ ($P = 0.0005$). No modifications of dynamin-related protein 1 (Drp1) were found in BMSCs^{FRDA} (Fig. 1, C and D). The reduced Mfn1 of treated BMSCs$^{FRDA\#1}$ and BMSCs$^{FRDA\#2}$ may help to segment damaged mitochondria, promoting their clearance by macroautophagy (*28*).

Because lipidation of Microtubule-associated protein 1A/1B-light chain 3 (LC3) and its association with autophagosome membranes has been established as a useful sign for autophagy, we detected LC3 by immunoblotting. A significant increase in LC3II/LC3I ratio was found in both BMSCs$^{FRDA\#1}$ ($P = 0.0004$) and BMSCs$^{FRDA\#2}$ ($P = 0.0016$) compared to BMSCs$^{CTR\#1}$ and BMSCs$^{CTR\#2}$ (Fig. 1, C and D). On the other hand, the LC3II/LC3I ratio of Au_8-pX–treated BMSCs$^{FRDA\#1}$ and BMSCs$^{FRDA\#2}$ cells was significantly lower than their base line conditions, at both 5 μM ($P = 0.0092$ and $P = 0.0003$, respectively) and 10 μM Au_8-pX ($P = 0.0018$ and $P = 0.0011$, respectively) (Fig. 1, C and D). Increased expression of Autophagy related 7 (Atg7), required for activation of LC3II and other ubiquitin-like substrates in the autophagy pathway (*10*), was found in untreated BMSCs$^{FRDA\#1}$ and BMSCs$^{FRDA\#2}$ compared to the BMSCs$^{CTR\#1}$ and BMSCs$^{CTR\#2}$ ($P = 0.0024$ for BMSCs$^{FRDA\#1}$ and $P = 0.0035$ for BMSCs$^{FRDA\#2}$) (Fig. 1, C and D). The administration of Au_8-pXs significantly reduced the Atg7 expression in BMSCs$^{FRDA\#1}$ and BMSCs$^{FRDA\#2}$ comparable to respective BMSCs^{CTR} (5 μM Au_8-pXs: $P = 0.0033$ for treated BMSCs$^{FRDA\#1}$ and $P = 0.0042$ for treated BMSCs$^{FRDA\#2}$; 10 μM Au_8-pXs: $P = 0.0038$ for treated BMSCs$^{FRDA\#1}$ and $P = 0.0049$ for treated BMSCs$^{FRDA\#2}$). We then determined the ubiquitin-binding protein p62 (p62) protein accumulation, a selective substrate of autophagy, to evaluate the activation of the autophagic flux (*10*). As shown in Fig. 1C, a significant increase in p62 was detected in both BMSCs$^{FRDA\#1}$ ($P = 0.0005$) and BMSCs$^{FRDA\#2}$ ($P = 0.0062$) in comparison with respective BMSCs^{CTR}, indicating impairment in the autophagic flux. Furthermore, p62 was significantly decreased in Au_8-pX–treated BMSCs$^{FRDA\#1}$ and BMSCs$^{FRDA\#2}$ cells compared to the untreated BMSCs^{FRDA} (5 μM Au_8-pXs: $P < 0.0001$ for treated BMSCs$^{FRDA\#1}$ and $P < 0.0001$ for treated BMSCs$^{FRDA\#2}$; 10 μM Au_8-pXs: $P < 0.0001$ for treated BMSCs$^{FRDA\#1}$ and $P < 0.0001$ for treated BMSCs$^{FRDA\#2}$), suggesting a recovery of the autophagic flux. During unbalanced redox homeostasis, the p62 increases the availability and function of Nrf2—a master regulator of antioxidant enzyme expression similar to glutathione peroxidase-1 (GPx-1) (*29*). Au_8-pX concentration–dependent increase of Nrf2 was observed in BMSCs$^{FRDA\#1}$ (Fig. 1, C and D) (5 μM Au_8-pXs: $P = 0.0275$; 10 μM Au_8-pXs: $P = 0.002$ versus untreated BMSCs$^{FRDA\#1}$). Nrf2 was significantly less expressed in untreated BMSCs$^{FRDA\#1}$ and BMSCs$^{FRDA\#2}$ cells compared to BMSCs^{CTR} ($P = 0.0375$ and $P = 0.0104$, respectively) (Fig. 1, C and D). Hence, we asked whether the recovery of the autophagic flux and Nrf2 may increase the expression of FXN. The FXN transcript is translated into a cytosolic precursor protein (pFXN) that is rapidly imported into mitochondria, to be further processed from an intermediate form (iFXN) to a mature protein (mFXN), resident in the mitochondrial matrix (*30*). We found that Au_8-pX treatment increased the expression of total FXN in BMSCs$^{FRDA\#1}$ and BMSCs$^{FRDA\#2}$ cells in a dose-dependent manner (Fig. 1, C and D). The mFXN expression was robustly increased in Au_8-pX–treated BMSCs$^{FRDA\#1}$ (5 μM Au_8-pXs: $P = 0.0168$; 10 μM Au_8-pXs: $P < 0.0001$ versus untreated BMSCs$^{FRDA\#1}$) compared to BMSCs$^{FRDA\#2}$ cells (5 μM Au_8-pXs: $P = 0.0306$; 10 μM Au_8-pXs: $P = 0.0166$ versus untreated BMSCs$^{FRDA\#2}$), where we also noted an unexpected increase of iFXN expression of treated and untreated BMSCs$^{FRDA\#2}$ compared to BMSCs$^{CTR\#2}$ (BMSCs$^{FRDA\#2}$: $P = 0.0402$; 5 μM Au_8-pX BMSCs$^{FRDA\#2}$: $P = 0.0151$; 10 μM Au_8-pX BMSCs$^{FRDA\#2}$: $P = 0.0162$) (Fig. 1, C and D). We next examined the autophagic flux of BMSCs$^{FRDA\#1}$ analyzing LC3 turnover using starvation as autophagy inducer and bafilomycin A1 (Baf-A1), which inhibits the autophagosome-lysosome fusion (Fig. 2). Starvation alone did not increase LC3II expression; however, starvation + Baf-A1 and bafilomycin alone increased LC3II compared to nontreated BMSCs$^{FRDA\#1}$ (Baf-A1: $P = 0.0216$ at 2 hours and $P = 0.0331$ at 4 hours; starvation + Baf-A1: $P = 0.0445$ at 2 hours and $P = 0.0285$ at 6 hours) (Fig. 2A). An increased accumulation of p62 was found both in Baf-A1 and in starvation + Baf-A1–treated BMSCs$^{FRDA\#1}$ (Baf-A1: $P = 0.008$ at 2 hours and $P = 0.0047$ at 6 hours; starvation + Baf-A1: $P = 0.0061$ at 2 hours and $P = 0.0466$ at 6 hours) with no differences in Atg7 expression, reflecting a loss of the autophagic flux of BMSCs$^{FRDA\#1}$ (Fig. 2A). To clarify whether FXN downregulation triggers disruption of the autophagy flux, we performed experiments with BMSCs$^{FRDA\#1}$ transduced for the expression of FXN [Lentiviral (LV)–FRDA#1]. Although LV-FRDA#1 cells showed simultaneous decrease of p62 and LC3II/LC3I ratio, lentivirus-mediated FXN expression was not sufficient to recover autophagic flux and required further investigations (Fig. 2B). In addition, the autophagic markers of Au_8-pX–treated LV-FRDA#1 cells remained similar to untreated LV-FRDA#1 cells (Fig. 2C). Overall, these results suggest a role of autophagy in FRDA and show that Au_8-pX treatment determines a recovery of the mitochondria fusion leading to a rescued autophagic flux with consequent increase in FXN protein expression.

Recovery of the mitochondrial bioenergetic function in cells from patients with FRDA treated with Au_8-pXs

Because the bone marrow environment is severely affected by iron overload and ROS that harm mitochondrial morphology and function during proliferation of BMSCs (*31*, *32*), they likely represent a model of cells highly sensitive to FXN deficiency. 3-(4,5-dimethylthiazol-2-yl)-2,5-diphenyltetrazolium bromide (MTT) assays indicated that the viability of BMSCs$^{FRDA\#1}$ was decreased compared to both BMSCs^{CTR} and BMSCs$^{FRDA\#2}$ (fig. S2B) (24 hours: $P = 0.0001$ and $P < 0.0001$; 48 and 72 hours: $P < 0.0001$ and $P < 0.0001$, respectively). To a lesser degree, BMSCs$^{FRDA\#2}$ displayed a slow growth becoming

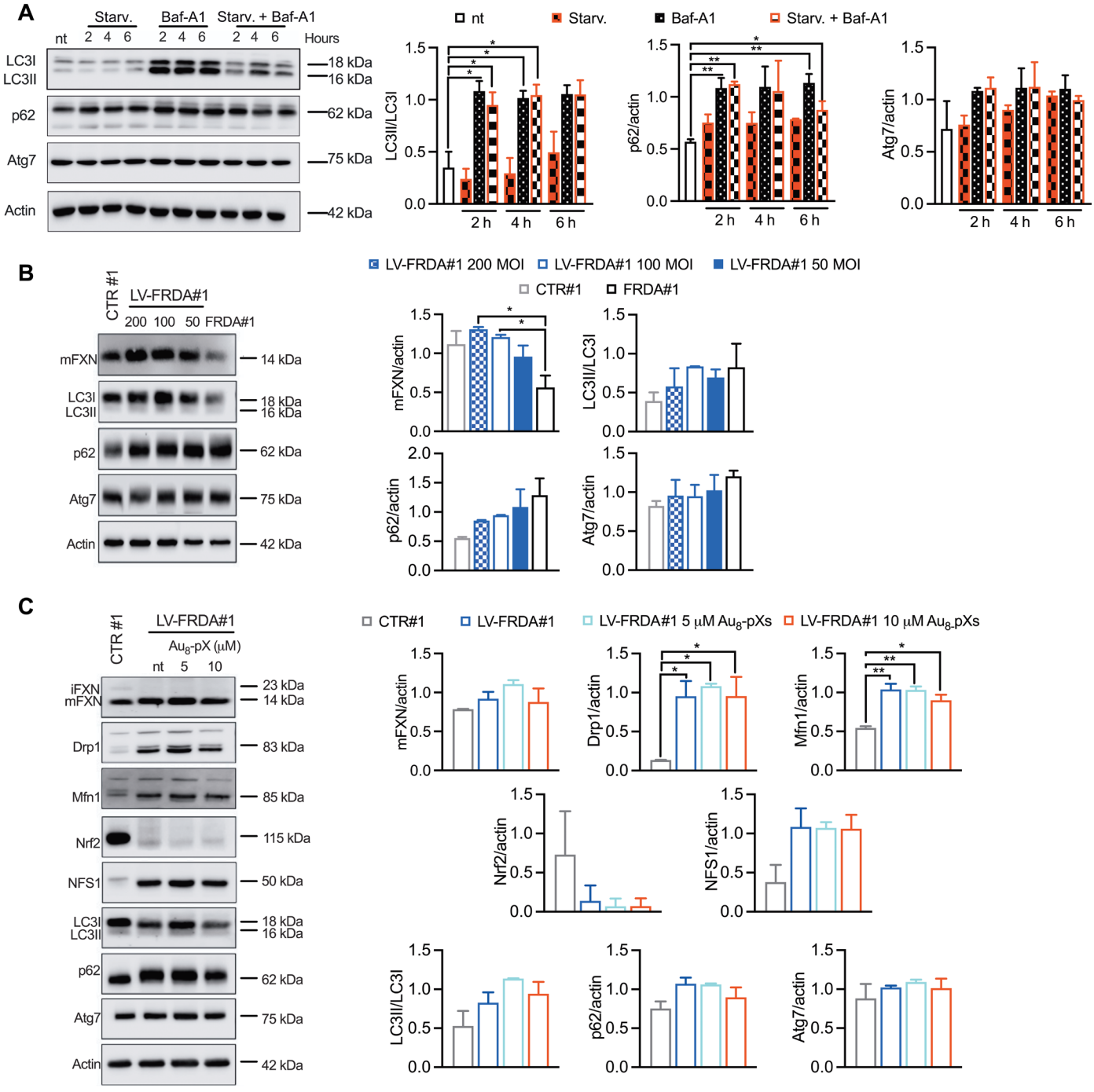

Fig. 2. Frataxin expression modulates impaired autophagy in FRDA-derived BMSCs. (**A**) BMSCs$^{FRDA\#1}$ cells were treated with serum deprivation (starvation), 400 nM bafilomycin (Baf-A1) or starvation, and 400 nM Baf-A1 for 2, 4, and 6 hours. Untreated (nt) BMSCs$^{FRDA\#1}$ cells were used as control. Cell lysates were subjected to LC3, p62, and Atg7 immunoblots. Densitometric analyses are shown as normalization on actin as loading control. (**B**) BMSCs$^{FRDA\#1}$ cells were then transduced with a full-length FXN expressing lentiviral vector (LV-EF1a-FXN-GFP) at 50, 100, and 200 multiplicity of infection (MOI), and lysates were analyzed by immunoblotting with frataxin (mature protein FXN), LC3, p62, and Atg7. Healthy (CTR#1) and not transfected BMSCs$^{FRDA\#1}$ cells (FRDA#1) were used as control. Densitometric analyses are shown as normalization on actin as loading control. (**C**) Representative Western blots of frataxin (mature protein mFXN) and FXN-related proteins (Nrf2 and NFS1), mitochondrial fusion (Mfn1) and fission (Drp1) proteins, and proteins related to the autophagic flux (LC3I, LC3II, p62, and Atg7) in Au_8-pX–treated and untreated (nt) LV-FRDA#1 cells. BMSCs from age-matched healthy donors (CTR#1) were evaluated as controls. Actin was used as loading control for densitometric analyses. Data were expressed as means ± SD ($n = 2$ independent experiments); $^*P < 0.05$ and $^{**}P < 0.01$ (ordinary one-way ANOVA, Bonferroni's test).

significantly related to CTR at 72 hours (P = 0.0001; fig. S2B). These findings suggested that FXN deficiency somehow impairs BMSC$^{FRDA\#1}$ proliferation possibly by reducing metabolic activity. We thus chose to use BMSCs$^{FRDA\#1}$ as the line most representative for cell vulnerability in FRDA. BMSCs$^{FRDA\#1}$ largely benefited from Au_8-pX uptake, and, at both doses, cells grew faster than untreated cells starting from 12 hours of IncuCyte living-cell analysis (12 hours: $P < 0.0001$ for BMSCs$^{FRDA\#1}$, 5 μM Au_8-pXs and $P = 0.0009$ for BMSCs$^{FRDA\#1}$, 10 μM Au_8-pXs; from 18 up to 48 hours: $P < 0.0001$ for both Au_8-pX treatment) (Fig. 3A). Considering the diverse cellular adaptation depending on cluster molarity, we next assessed the in vitro release of ROS from BMSCs$^{FRDA\#1}$ treated with 5 and 10 μM of Au_8-pXs for 24 hours. We observed significantly higher amounts of ROS in untreated BMSCs^{FRDA} compared to BMSCs^{CTR} ($P < 0.0001$), which was rescued by treatment with Au_8-pXs at both molarity ($P < 0.0001$) (Fig. 3B). Again, we detected a more effective ROS scavenger activity of 5 μM Au_8-pXs ($P = 0.0095$) compared to 10 μM condition, for whose BMSCs$^{FRDA\#1}$ apparently have a less immediate response (Fig. 3B). For ROS evaluation, we measured the amount of H_2O_2 that is the ROS with the longest half-life and easiest to detect in vitro (*33*). However, it is important to highlight that there are other ROS, including superoxide, hydroxyl radical, and singlet oxygen, that can be enzymatically converted to H_2O_2 (*34*).

Frataxin deficiency hampered SOD signaling in patients with FRDA and animal models (*35*, *36*), leading to inefficient response to oxidative stress and a dysfunctional mitochondrial electron transport chain (ETC). In keeping with the highly preferential buffering activity of Au_8-pXs toward oxygen singlets and superoxide species, we sought for potential effects on mitochondrial metabolism and respiration. First, we used Seahorse Oxygen flow for the assessment of ETC functions. We found that BMSCs$^{FRDA\#1}$ had reduced basal and maximal respiratory capacity compared to BMSCs^{CTR} ($P = 0.0289$ and $P = 0.0031$, respectively) (fig. S2C). Au_8-pX–treated BMSCs$^{FRDA\#1}$ showed enhanced oxygen consumption rate compared to BMSCs$^{FRDA\#1}$ (Fig. 3C), which was most evident as basal ($P = 0.0471$ for 5 μM Au_8-pXs and $P = 0.0105$ for 10 μM Au_8-pXs) and uncoupled (maximal) respiration ($P < 0.0001$ for 5 μM Au_8-pXs and $P = 0.02$ for 10 μM Au_8-pXs) (Fig. 3D). Extracellular acidification rate (a measure of glycolysis)

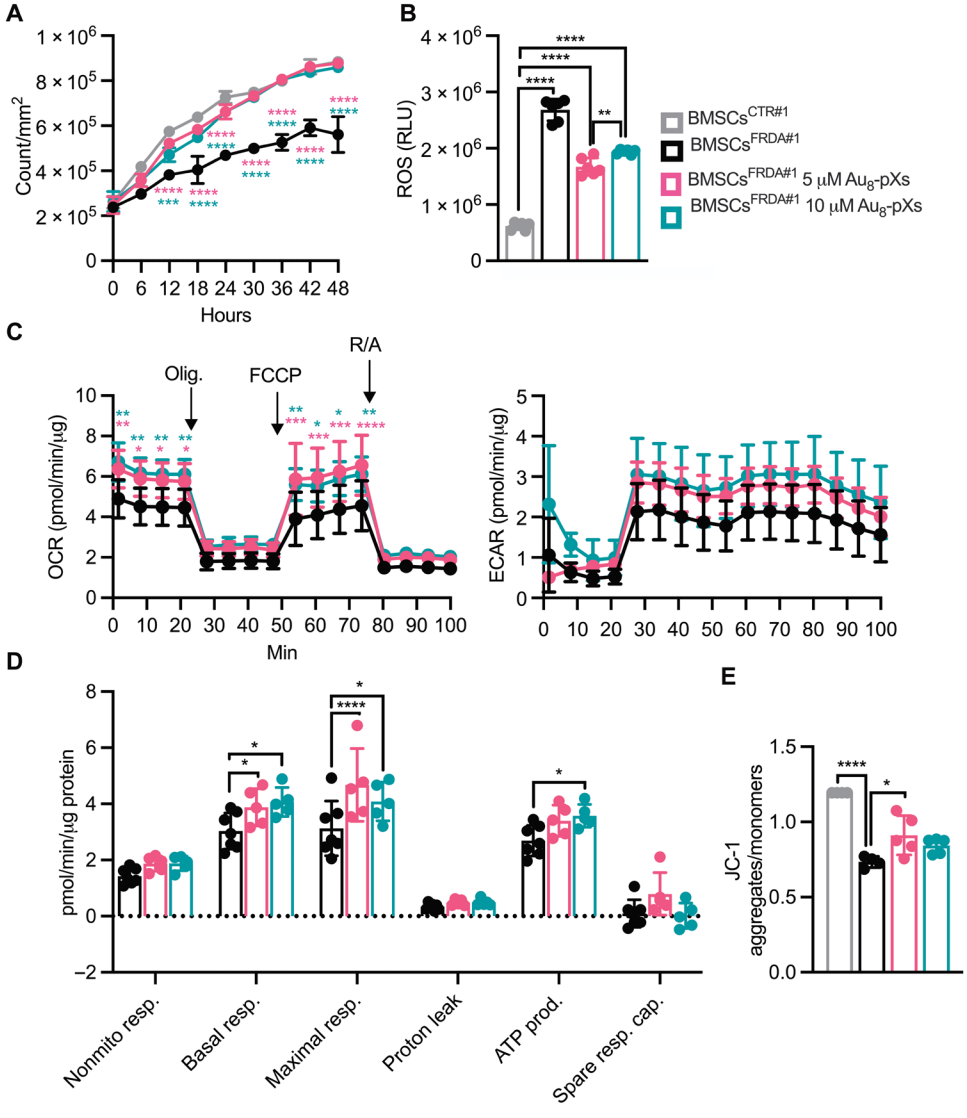

Fig. 3. Recovery of the mitochondrial bioenergetic function in FRDA-derived BMSCs treated with Au_8-pXs. (**A**) IncuCyte evaluation of proliferative capacities in 5 and 10 μM Au_8-pX–treated BMSCs$^{FRDA\#1}$, BMSCs$^{FRDA\#1}$, and BMSCs^{CTR}. Recording of object count/mm^2 was performed every 6 hours from Au_8-pX labeling of cells (hour 0) up to 48 hours. Data were expressed as means ± SD ($n = 3$ wells per group); ***$P < 0.001$ and ****$P < 0.0001$ (ordinary two-way ANOVA, Bonferroni's test). (**B**) Assessment of ROS in BMSCs$^{FRDA\#1}$ treated for 24 hours with 5 and 10 μM Au_8-pXs, untreated BMSCs$^{FRDA\#1}$, and BMSCs^{CTR}. ROS amount was expressed as relative light units (RLU). Data were expressed as means ± SD ($n = 3$ wells per group; $n = 2$ independent experiments); **$P < 0.01$ and ****$P < 0.0001$ (ordinary one-way ANOVA, Bonferroni's test). (**C**) Mitochondrial analysis of oxygen consumption rates (OCRs) and extracellular acidification rates (ECARs) in Au_8-pX–treated and untreated BMSCs$^{FRDA\#1}$ measured by XFp Extracellular Flux Analyzer Seahorse. Cells were subsequently treated with 2.5 μM oligomycin (Olig), 0.5 μM carbonyl cyanide *p*-trifluoromethoxyphenylhydrazone (FCCP), and 1 μM rotenone and antimycin (R/A). $n = 4$ measurements were recorded before each treatment. (**D**) Oxygen consumption rate measures were used to calculate nonmitochondrial respiration and basal and maximal respiratory capacity, as well as ATP production and spare respiratory capacity. (C and D) Data were expressed as means ± SD ($n = 5$ wells for Au_8-pX–treated BMSCs$^{FRDA\#1}$, $n = 7$ wells for BMSCs$^{FRDA\#1}$); *$P < 0.05$, **$P < 0.01$, ***$P < 0.001$, and ****$P < 0.0001$ (ordinary two-way ANOVA, Bonferroni's test). (**E**) Mitochondrial membrane potential (MMP) evaluation by the lipophilic dye JC-1. Statistical analysis of red/green ratio (green, monomeric form; red, aggregate) of fluorescence variation. Data were expressed as means ± SD ($n = 4$ wells for BMSCs^{CTR} and BMSCs$^{FRDA\#1}$, $n = 5$ wells for Au_8-pXs treated BMSCs$^{FRDA\#1}$); *$P < 0.05$ and ****$P < 0.0001$ (ordinary one-way ANOVA, Bonferroni's test).

was comparable among all conditions (Fig. 3C). In addition, 10 μM Au_8-pX administration sustained an enhanced oligomycin-inhibited respiration, which reflects the capacity for adenosine 5′-triphosphate (ATP) production compared to $BMSCs^{FRDA\#1}$ ($P = 0.0363$) (Fig. 3D). Last, we measured the mitochondrial membrane potential (MMP), as an indicator of mitochondrial integrity, by the lipophilic dye 5,5',6,6'-Tetrachloro-1,1',3,3'-tetraethylbenzimidazolylcarbocyanine iodide (JC-1) (*37*) (Fig. 3E). The increased ratio of red versus green fluorescence in $BMSCs^{FRDA\#1}$ cells after Au_8-pX treatment indicated more polarized mitochondria. All these data indicate that Au_8-pX treatment could rescue the bioenergetic function of $BMSCs^{FRDA\#1}$ cells.

Au_8-pX therapeutic effects in nervous and skeletal muscle systems of treated YG8sR mice

To examine whether Au_8-pXs were able to exert the ROS scavenging activity, and to trigger detoxifying pathways in a whole organism, we performed a single intravenous injection of Au_8-pXs into the tail vein of the YG8sR murine model of FRDA. YG8sR mice exclusively express two disease-causing human *FXN* transgenes (h*FXN*) containing GAA expansions, representing one of the most suitable and representative animal models of FRDA (*19*).

YG8sR mice ($n = 10$) were treated when they exhibited a substantial motor behavior decline (12 months of age) (*19*) and tested for 6 months after injection (18 months of age). To verify the cluster circulation and the penetration into murine tissues, YG8sR mice ($n = 6$) were injected with Au_8-pXs and euthanized after 30 ($n = 3$) or 180 days ($n = 3$). The gold content was evaluated by an inductively coupled plasma mass spectrometry (fig. S3A). A group of $n = 6$ untreated YG8sR mice was used for comparative analyses. At 30 and 180 days, heart, brain cortex and cerebellum, basal ganglia (BGs), muscles [quadriceps (QAs), tibialis anterior (TAs), and soleus (SL)], liver, lung, kidney, and pancreas were harvested for gold element content quantification (fig. S3A). Au_8-pX distribution pattern was not dependent on time, except for the liver where gold cluster superstructures highly accumulated within the first 30 days and underwent a slow hepatic clearance through time (*38*) ($P < 0.0001$, compared to 180 days). This finding suggested the long-term retention of Au_8-pXs within injected tissues that may be beneficial for single infusion–based treatments. Au_8-pXs preferentially entered QAs, cerebellum, liver, cortex, and TAs (fig. S3B). Au_8-pXs could penetrate the blood-brain barrier (BBB) and gain access to the brain (fig. S3B). This result was further confirmed by in vivo detection of intravenously injected Au_8-pXs by using intravital time-lapse laser confocal imaging. Vessels were visualized by a systemic administration of fluorescent antibody against CD31. In vivo images confirmed the migration of Au_8-pXs through the brain vessel walls, demonstrating that Au_8-pXs could pass the BBB and penetrate the surrounding tissues (fig. S3B).

Treatment with Au_8-pXs improves neuromotor, muscle, and cardiac functions in aged YG8sR mice

Before Au_8-pX treatment, neurological deficits were already apparent in the YG8sR mice compared to age-matched wild-type C57Bl controls. These deficits in the YG8sR mice became more prominent with increasing age (Fig. 4 and fig. S4). We then examined whether Au_8-pX administration could rescue or protect YG8sR mice from the progressive neurobehavioral and muscular deficit characterizing FRDA disease phenotype. Exhaustion and endurance time were evaluated by treadmill fatigue test, forcing mice to run with gradually increasing speed, whereas neuromuscular functions were assessed by forelimb grip strength test (Fig. 4, B and C). Functional measurements were performed in a blind-to-treatment assignment. Treadmill test results were expressed as total numbers of shocks received (Fig. 4B). We found that YG8sR mice were not able to sustain the exercise as demonstrated by the increased number of shocks, especially at medium- and high-speed test and over time. Au_8-pX–treated YG8sR mice were instead less prone to fatigue and displayed better treadmill performances, independently from the work intensity. The number of shocks was greatly reduced in Au_8-pX–treated YG8sR mice compared to YG8sR, starting from 20 days after treatment for medium ($P = 0.0001$) and high ($P = 0.0468$) running speeds, with improvement maintained 60 days ($P = 0.0191$, low intensity; $P < 0.0001$, medium intensity; $P = 0.0006$, high intensity), 90 days ($P = 0.0063$, low intensity; $P < 0.0001$, medium intensity; $P = 0.0003$, high intensity), and 120 days after injection ($P < 0.0001$, for all the running speeds). From 60 days, Au_8-pX–treated YG8sR mice displayed a treadmill performance comparable to wild-type mice, at any speed, suggesting that Au_8-pX administration could help to a great extent in improving fatigue resistance of YG8sR mice.

To gather further insights into neuromuscular functions, we performed forelimb grip strength test aiming at evaluating muscle properties, contractility, and strength, at 60 and 180 days after Au_8-pX injection (Fig. 4C). We found a general forelimb muscle strength increase in Au_8-pX–treated YG8sR mice, suggesting that gold cluster effects might be effective in improving muscle force, although neither outperforming nor reaching wild-type muscle force values (60 days, $P = 0.0338$ versus YG8sR and $P = 0.0004$ versus C57Bl; 180 days, $P = 0.0058$ versus YG8sR and $P < 0.0001$ versus C57Bl). In contrast, no differences of treadmill and grip strength data were observed comparing Au_8-pX–treated and untreated age-matched C57Bl mice, indicating the specificity of the effects of Au_8-pXs in YG8sR mouse FRDA model (fig. S4).

Enhanced fatigue resistance likely results from improved cardiac functions (*39*). To this end, we performed echocardiographic analyses in 18-month-old untreated and Au_8-pX–treated YG8sR mice (Fig. 4, D and E). The investigator performing the cardiac measurements was blinded to the identity of the treatment group. Transthoracic echocardiac image outcomes revealed enhanced heart contractile functions in Au_8-pX–treated YG8sR mice, as demonstrated by increased left ventricular ejection fraction (EF) ($P = 0.0042$) and fractional shortening (FS) ($P = 0.0088$) compared to YG8sR mice (Fig. 4D). These data were confirmed by the significant increase of the left ventricular outflow (LV CO) and stroke volume in Au_8-pX–treated YG8sR mice (Fig. 4E) ($P < 0.0001$), suggesting more physiological hemodynamic conditions in Au_8-pX–treated compared to untreated YG8sR mice. However, Au_8-pX treatment was not able to completely rescue the YG8sR heart contractility to the physiological values observed in C57Bl mice (EF %: $P = 0.0087$ versus C57Bl; FS %: $P = 0.0199$ versus C57Bl). Moreover, other measurements, such as cardiac chamber dimensions and functions (Fig. 4E and table S2), suggested no major myocardial remodeling.

QAs and hearts of Au_8-pX–treated YG8sR mice showed reduced LC3II/LC3I ratio ($P = 0.0011$ for QAs and $P = 0.0404$ for heart), decreased Atg7 expression ($P = 0.0065$ for QAs and $P < 0.0001$ for heart), and increased accumulation of p62 in hearts ($P = 0.0421$) compared with untreated group (Fig. 4F and fig. S5). Moreover, the Au_8-pX treatment induced significant decrease of NFS1 in QAs ($P = 0.0061$) and hearts ($P = 0.0002$) and did not affect Nrf2 in both tissues (Fig. 4F and fig. S5). Subsequently, we investigated whether Au_8-pX treatment

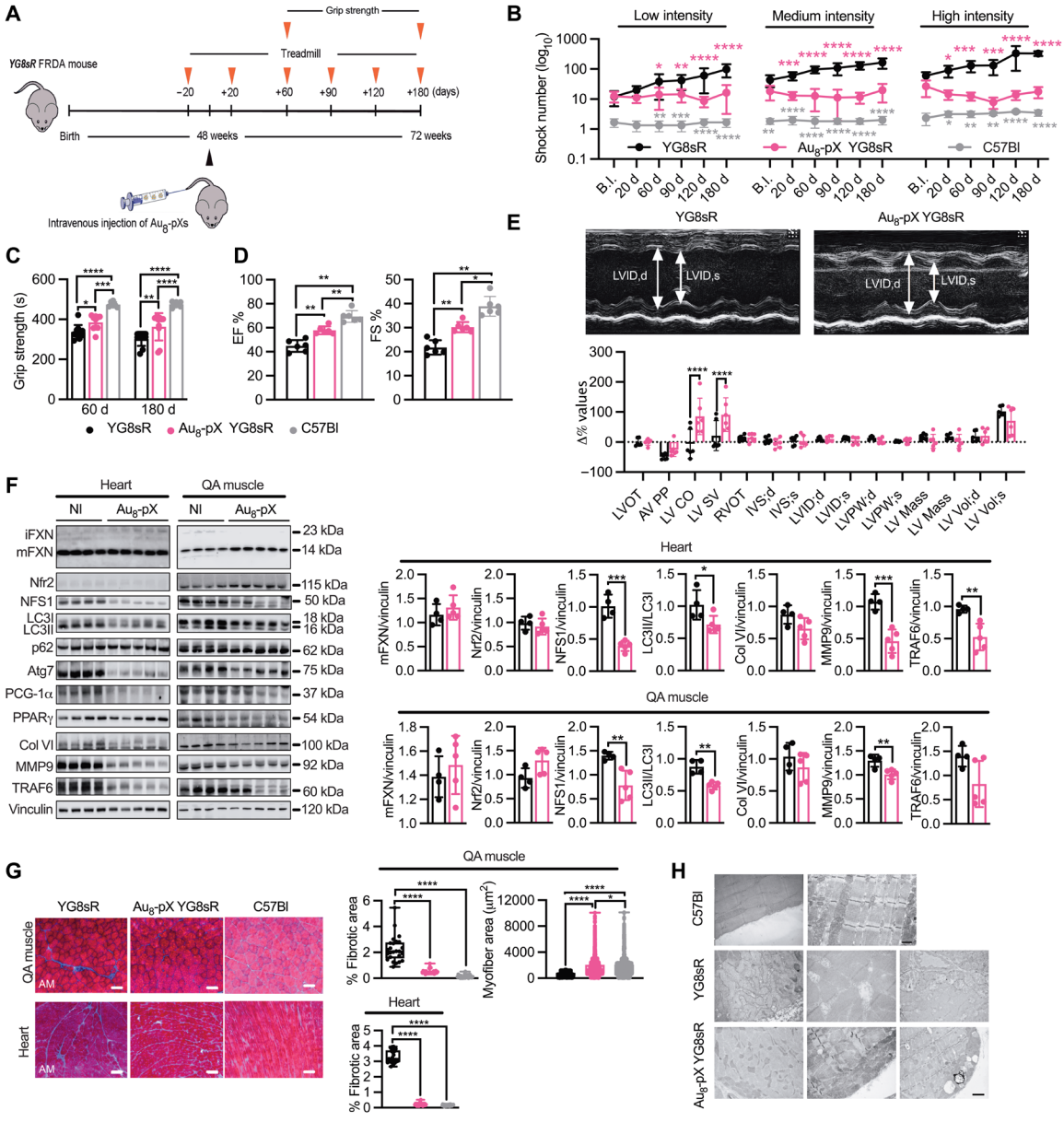

Fig. 4. Au_8-pX therapeutic effects in skeletal and cardiac muscles of treated YG8sR mice. (**A**) Schematic of Au_8-pX intravenous injection into 12-month-old YG8sR mice (Au_8-pX YG8sR; $n = 10$) and functional measurement evaluation time points. Untreated YG8sR mice ($n = 10$) and C57Bl mice ($n = 6$) were examined at the same time points. (**B**) Treadmill performance of Au_8-pX YG8sR ($n = 10$), YG8sR ($n = 10$), and C57Bl ($n = 6$) mice for three different experimental conditions: low intensity (38 cm/s), medium intensity (42 cm/s), and high intensity (46 cm/s). Results from the onset of pathological signs (B.I., Before Injection) to the sacrifice day were displayed and expressed as averaged number of shocks ± SD. (**C**) Outcomes from grip strength test 60 and 180 days after Au_8-pX injection ($n = 10$ Au_8-pX YG8sR mice, $n = 10$ YG8sR, and $n = 6$ C57Bl mice). Data were expressed as means ± SD. (**D** and **E**) Percentage of ejection fraction (EF) and fractional shortening (FS) was calculated from echocardiography images performed on Au_8-pX YG8sR ($n = 6$) and YG8sR ($n = 6$) mice before the sacrifice. Values were compared to EF % and FS % of C57Bl mice ($n = 6$). Percentage of EF and FS were expressed as means ± SD. Other echocardiography measures were acquired and expressed as delta percentage (Δ%) of Au_8-pX YG8sR and YG8sR values ($n = 6$ mice per group). (B, C, and E) Statistical analyses were performed with ordinary two-way ANOVA followed by Bonferroni's test. (D) Statistical analyses were performed with ordinary one-way ANOVA followed by Bonferroni's test; $^*P < 0.05$, $^{**}P < 0.01$, and $^{****}P < 0.0001$. (**F**) Representative Western blots of frataxin (intermediate form iFXN and mature protein mFXN) and FXN-related proteins (Nrf2, NFS1, PGC-1α, and PPARγ), proteins related to the autophagic flux (LC3I, LC3II, p62, and Atg7) and fibrosis deposition (Col VI and MMP9), and tumor necrosis factor receptor–associated factor 6 (TRAF6) in QAs and hearts of Au_8-pX YG8sR ($n = 5$) and YG8sR ($n = 4$) mice. Vinculin was used as loading control. Densitometric analyses of biological markers (mFXN, Nrf2, NFS1, LC3II/LC3I, Col VI, MMP9, and TRAF6) are shown as normalization on vinculin. Data were expressed as means ± SD of $n = 2$ independent experiments; $^*P < 0.05$, $^{**}P < 0.01$, and $^{***}P < 0.001$ (unpaired Student's t test). (**G**) Representative images of QAs and hearts from Au_8-pX YG8sR, YG8sR, and C57Bl mice stained with Azan Mallory for fibrosis detection ($n = 5$ Au_8-pX YG8sR, $n = 5$ YG8sR, and $n = 5$ C57Bl mice; $n = 5$ sections for each mouse). Scale bars, 200 μm. Tissue fibrosis in QAs and hearts and QA myofiber area (μm^2) were quantified by ImageJ ($n = 5$ Au_8-pX YG8sR, $n = 5$ YG8sR, and $n = 5$ C57Bl mice; $n = 5213$ values for each mouse). Data were represented as box-and-whisker plots: Boxes indicate 25th to 75th percentiles, and whiskers extend from the minimum to maximum values; lines indicate median. Statistical analyses were performed with unpaired Student's t test; $^*P < 0.05$, $^{****}P < 0.0001$. (**H**) Electron microscopy images of thin sections from QAs of Au_8-pX YG8sR, YG8sR, and C57Bl mice ($n = 3$ mice per group). Scale bar, 1 μm for C57Bl and 2 μm for Au_8-pX YG8sR and YG8sR.

modulates the activity of the PGC-1α as a critical regulator that links metabolic activity to relevant environmental stimuli in multiple pathways affected in FRDA (*40*). A significant decrease of PGC-1α was observed in hearts and QAs of Au_8-pX–treated YG8sR mice ($P = 0.0063$ for hearts and $P = 0.0270$ for QAs) (Fig. 4F and fig. S5, A and B). PPARγ was significantly decreased in QAs of Au_8-pX–treated YG8sR mice ($P = 0.00132$) (Fig. 4F and fig. S5B). The expression of mFXN in QAs and hearts of Au_8-pX–treated YG8sR mice remained unchanged (Fig. 4F). Furthermore, no differences in autophagy, NFS1/Nrf2, or PGC-1α– and PPARγ–related pathways were observed comparing age-matched Au_8-pX–treated and C57Bl mice, in agreement with the normal expression of FXN (fig. S4).

Despite the fact that skeletal muscle fibrosis is not considered an overt hallmark of YG8sR, in line with the mild and variable myopathic features of muscles from patients with FRDA, morphometric analysis of QAs from Au_8-pX–treated YG8sR mice showed decreased collagen deposition compared to untreated mice ($P < 0.0001$ for Au_8-pX–treated YG8sR versus YG8sR) (Fig. 4G). Moreover, QA myofibers displayed markedly smaller cross-sectional areas (CSAs) in the untreated YG8sR mice compared to those that received Au_8-pXs (YG8sR CSA mean of 607.99 ± SD of 304 μm^2; Au_8-pX–treated YG8sR CSA mean of 1520.10 ± SD of 1092.45 μm^2; C57Bl CSA mean of 1565.34 ± SD of 1176.24 μm^2) ($P < 0.0001$ for Au_8-pX–treated YG8sR mice versus YG8sR and YG8sR versus C57Bl; $P = 0.0431$ for Au_8-pX–treated YG8sR mice versus C57Bl) (Fig. 4G), indicating an unforeseen mechanism of myofiber atrophy rescue mediated by the Au_8-pX presence.

Pathophysiological signs of cardiac fibrosis and hypertrophy have been also shown to be positively affected by Au_8-pX injection (Fig. 4G). Azan Mallory staining of hearts showed only a mild accumulation of collagen and perivascular fibrosis in 18-month-old Au_8-pX–treated YG8sR mice, whereas aged YG8sR mice revealed disorganized cardiomyocytes and interstitial and perivascular myocardial fibrosis ($P < 0.0001$ for Au_8-pX–treated YG8sR versus YG8sR) (Fig. 4G). Overall, fibrogenic markers were elevated in hearts of YG8sR mice compared with Au_8-pX–treated YG8sR mice, which displayed a significant reduction of Matrix metallopeptidase 9 (MMP9) ($P = 0.0007$) and tumor necrosis factor receptor–associated factor 6 (TRAF6; $P = 0.0052$) markers (Fig. 4F and fig. S5A). Likewise, MMP9 fibrotic player was diminished in QAs of Au_8-pX–treated YG8sR ($P = 0.0074$) (Fig. 4F and fig. S5B). The reduction of cardiac fibrosis in Au_8-pX–treated YG8sR mice may explain the general improvement in both diastolic and systolic, function, and heart contractile properties.

Next, we explored the maintenance of a functional mitochondrial network, whose content and shape contribute to muscle mass, homeostasis, and metabolism (*41*). Qualitative analysis of electron microscopy images of YG8sR muscle showed a fusion network of swollen mitochondria with tubular morphology and large organelles (Fig. 4H). Conversely, mitochondria in C57Bl and YG8sR Au_8-pX–treated QA muscles exhibited a similar small and rounded shape with regular invagination of the inner membranes (Fig. 4H).

We sought to test whether Au_8-pX treatment could alleviate ataxia in FRDA pathology. Balance and motor coordination impairments, occurring largely in YG8sR mouse, were evaluated by footprint test and rotarod (Fig. 5, A and C). The investigators performing these analyses were blinded to the identity of the treatment group. Motor coordination and locomotor activity in Au_8-pX–treated and untreated YG8sR mice were assessed at 60, 120, and 180 days after injection (Fig. 5A). Au_8-pXs determined a rescue of gait alterations over time, especially at 180 days, when Au_8-pX–treated YG8sR mouse performance matched wild-type values both in stride length ($P < 0.0001$ versus YG8sR) and width evaluation ($P = 0.0206$ versus YG8sR), highlighted by the footprint pattern ascribable to a high balance and coordination (Fig. 5B). Consistent with the amelioration in gait analysis, balance improvement was found in Au_8-pX–treated YG8sR mice 180 days after injection, when rotarod test outcomes confirmed a latency to fall significantly higher than in untreated mice, and comparable to wild-type outcomes ($P = 0.0005$ versus YG8sR) (Fig. 5C). Rotarod performances did not display changes in untreated and Au_8-pX–treated wild-type mice (fig. S4, B and C).

Because both gait coordination and rotarod test give hints for determining a cerebellum-dependent coordination of motor movements (*10*), we complemented these neurofunctional studies with Western blot and immunofluorescence analysis with a focus on cerebellar tissue. To determine whether the autophagy pathway was activated in degenerating Purkinje cells in YG8sR mice, we performed LC3/p62/Atg7 Western blot analysis on cerebellar lysates from 18-month-old untreated and Au_8-pX–treated YG8sR mice (Fig. 5D and fig. S5C). The cerebellum of Au_8-pX–treated YG8sR mice showed reduced LC3II/LC3I ratio compared with untreated group ($P = 0.0284$) (Fig. 5D), with no changes in Atg7 and p62 expression (fig. S5C). In addition, NFS1 was significantly elevated in cerebellum of Au_8-pX–treated YG8sR mice ($P = 0.0117$), in association to an increased expression of PGC-1α ($P = 0.0043$) and decreased PPARγ protein ($P = 0.013$) (Fig. 5D and fig. S5C). All these proteins did not show different expression after Au_8-pX treatment of C57Bl mice (fig. S4) but were coincident with an increase of mFXN in cerebellum of Au_8-pX–treated YG8sR mice ($P = 0.0065$) (Fig. 5D). Together, these results indicate a reverse of autophagic flux impairment and restoration of some of the antioxidant signaling events in cerebellum after Au_8-pX treatment. Cerebellar Purkinje cells are enriched for FXN protein expression and undergo notable damage in samples from patients with FRDA and animal models (*42*). The Au_8-pX treatment reduced neuronal loss within the cerebellar dentate nucleus with an amplification of the pool of calbindin-positive Purkinje cell layer compared to YG8sR mice ($P < 0.0001$) (Fig. 5E), although without completely repopulating the calbindin cell layer of wild-type cerebellum ($P < 0.0001$ versus C57Bl). Consistent with previous studies (*7*), the number of Purkinje cells immunoreactive for parvalbumin, a calcium-binding protein that regulates neuronal firing properties (*43*), was reduced in YG8sR mice, whereas the number of these cells was significantly improved in Au_8-pX–treated YG8sR mice ($P < 0.0001$) (Fig. 5, F and G). No differences in the number of parvalbumin-positive cells were found between Au_8-pX–treated YG8sR and C57Bl mice. Moreover, GPx-1 staining quantification showed a reduction of immunoreactivity in Au_8-pX–treated mice ($P < 0.0001$ versus YG8sR) and a predominant localization around vessels of microglia (Fig. 5E). All these histopathological findings, together with the motor-functional results, indicate that Au_8-pX treatment is capable of blunting neurological disease in YG8sR mice.

Treatment with Au_8-pXs does not affect glucose intolerance in aged YG8sR mice

Diabetes mellitus and glucose intolerance are additional non-neurological symptoms affecting patients with FRDA (*44*) that have been attributed to pancreas degeneration determined by senescence pathway and apoptotic processes occurring in insulin-producing β cells. In addition, a high percentage of patients with FRDA have muscle insulin resistance (*45*), which can be a complementary cause of

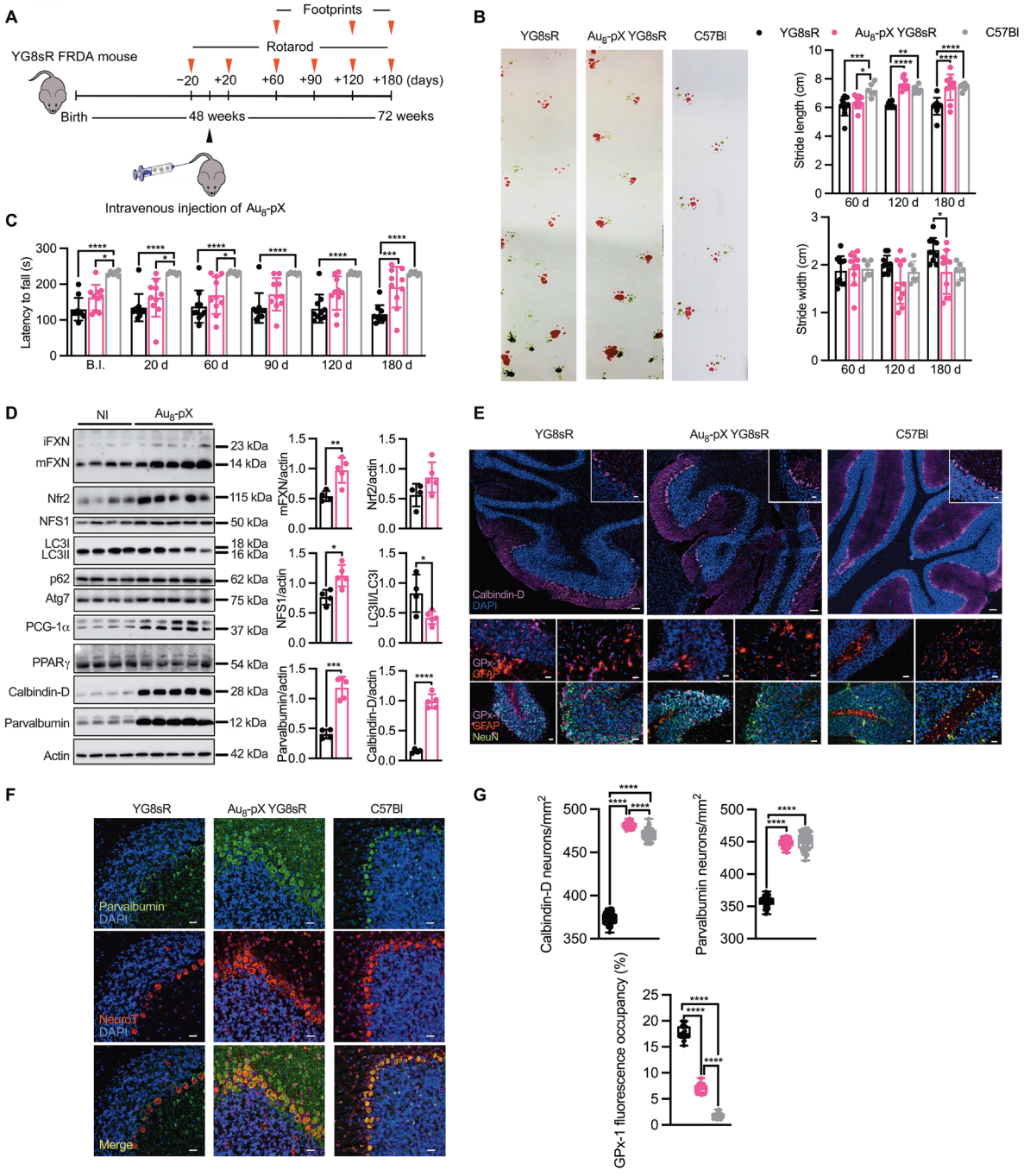

Fig. 5. Au_8-pX therapeutic effects in nervous systems of treated YG8sR mice. (**A**) Schematic of Au_8-pX intravenous injection into 12-month-old YG8sR mice and functional measurement time points. (**B**) Stride length and width from footprint tests performed on Au_8-pX YG8sR ($n = 10$), YG8sR ($n = 10$), and C57Bl ($n = 6$) mice after 60, 120, and 180 days from Au_8-pX injection. (**C**) Rotarod balance coordination of Au_8-pXs–injected YG8sR ($n = 10$), YG8sR ($n = 10$), and C57Bl ($n = 6$) mice from the onset of pathological signs (B.I.) to the sacrifice day. (B and C) Data were expressed as means ± SD; $^*P < 0.05$, $^{***}P < 0.001$, and $^{****}P < 0.0001$ (ordinary two-way ANOVA, Bonferroni's test). (**D**) Representative Western blot of frataxin (intermediate form iFXN and mature protein mFXN) and FXN-related proteins (Nrf2, NFS1, PGC-1α, and PPARγ), proteins related to the autophagic flux (LC3I, LC3II, p62, and Atg7), and Purkinje cells (parvalbumin and calbindin-D) in cerebellum lysates of Au_8-pX YG8sR ($n = 5$) and YG8sR ($n = 4$) mice. Densitometric analyses of biological markers (mFXN, Nrf2, NFS1, LC3II/LC3I, calbindin-D, and parvalbulmin) are shown as normalization on actin as loading control. Data were expressed as means ± SD of $n = 2$ independent experiments; $^*P < 0.05$, $^{**}P < 0.01$, $^{***}P < 0.001$, and $^{****}P < 0.0001$ (unpaired Student's t test). (**E** and **F**) Representative confocal images of cerebella from Au_8-pX YG8sR, YG8sR, and C57Bl mice stained for parvalbumin, calbindin-D, NeuroT, and NeuN for neurons and Purkinje cells, glial fibrillary acidic protein (GFAP) for microglia, and glutathione peroxidase-1 (GPx-1). Scale bars, 100 μm for calbindin-D tile scan (inset magnification of 10 μm) and 25 μm for the other fluorescence staining in (E) and (F). DAPI, 4′,6-diamidino-2-phenylindole. (**G**) Calbindin- and parvalbumin-positive cells were manually counted per square millimeter, and quantification of Gpx-1 staining was performed by ImageJ and expressed as percentage occupancy of the fluorescence labeling ($n = 5$ sections for each mouse; $n = 5$ mice per group). Data were expressed as means ± SD; $^{****}P < 0.0001$ (unpaired Student's t test).

hyperglycaemia, reduced glucose uptake, and poor exercise performance. Because YG8sR animal models resemble some aspects of patients' impaired glucose metabolism (*19*, *44*), we performed fasting glucose [glucose tolerance test (GTT)] and insulin [insulin tolerance test (ITT)] tolerance to verify a role of Au_8-pXs in increasing muscle insulin sensitiveness and endurance (fig. S6). In GTT experiments, Au_8-pX–treated and untreated YG8sR mouse glycemia was recorded before (as baseline) and up to 1 hour after glucose injection (1 mg/g). Baseline blood glucose concentrations from both groups were kept within normal ranges (<200 mg/dl) throughout 180 days of the experiments, indicating a condition probably preceding overt diabetes (fig. S6A). However, YG8sR mice showed concentration of blood glucose ≥200 mg/dl after glucose injection, suggesting a mild glucose intolerance (fig. S6A). There were no significant differences in GTT and ITT parameters between Au_8-pX–treated and untreated YG8sR mice (fig. S6, A and B). Therefore, our findings are consistent with a mild glucose intolerance in YG8sR mice that do not appear to respond to the Au_8-pX treatment.

Au_8-pX treatment restores physiological stress and redox pathways in YG8sR mice

We next sought for mitochondrial functions and changes of oxidative stress and damage parameters in Au_8-pX–treated YG8sR mouse tissues. We found increased mRNA of genes coding for antioxidant proteins such as *peroxyredoxin* (*Prdx2*) ($P < 0.0001$), *glutathione-S-transferase* (*Gstm1*) ($P = 0.0008$), and *Nrf2* ($P = 0.0102$) in the dorsal root ganglia of Au_8-pX–treated YG8sR mice (fig. S7A), commonly presenting severe injury (*46*). Along with these results, there was a general but variable increase of antioxidant enzymes mRNAs in the central nervous system (CNS; cortex, cerebellum, and BGs), suggesting priming of mobilization of defenses against oxidative stress (fig. S7A). We next investigated the cumulative damaging effects of ROS in tissue samples of the CNS, skeletal muscles, and hearts of Au_8-pXs–injected mice (fig. S7B). Total lysates of the CNS and skeletal muscles from the Au_8-pX–treated mice showed a significant reduction of 4-hydroxylnonenale (4-HNE), a stable product of lipid peroxidation, and 8-oxo-deoxy-guanosine (8-oxodG), a stable product of ROS-dependent DNA damage, compared to untreated samples, suggesting the restoration of redox regulation state found in C57Bl (4-HNE total lysate: $P < 0.0001$ for cortex, cerebellum, QA, and TA; BGs: $P = 0.0163$; SL: $P = 0.0002$) (8-oxodG total lysate: $P < 0.0001$ for cortex, cerebellum, QA, and TA; BGs: $P = 0.0170$; SL: $P = 0.0065$). A similar pronounced decrease of 4-HNE amount was found in CNS and skeletal muscle mitochondrial extracts from Au_8-pXs–injected YG8sR compared to the untreated mice, whereas lower 8-oxodG concentration was restricted to cerebellum and skeletal muscles (4-HNE mitochondrial extracts: cortex: $P = 0.0002$; BGs: $P = 0.0014$; cerebellum and SL: $P < 0.0001$; QA: $P = 0.0002$; TA: $P = 0.0075$) (8-oxodG mitochondrial extract: cerebellum: $P = 0.0003$; QA: $P < 0.0001$; TA: $P = 0.0022$; SL: $P = 0.0123$) (fig. S7B). No differences in both parameters were found in YG8sR-treated hearts, suggesting the occurrence of tissue-specific abilities to mount antioxidant strategies with different rate and efficiency.

Consistent with a reduced requirement and/or consumption of the antioxidant molecules, Au_8-pX–treated YG8sR and wild-type mice showed significant higher amounts of glutathione (reduced form) (GSH) compared to YG8sR mice in cortex ($P = 0.0161$ and $P < 0.0001$), BGs ($P = 0.0006$ and $P = 0.0045$), QA ($P = 0.0046$ and $P = 0.0003$), and TA ($P = 0.0163$ and $P = 0.0015$) (fig. S7C). In addition, GSH cerebellum was significantly higher in Au_8-pX–treated YG8sR than YG8sR mice ($P = 0.0130$) (fig. S7C). Similarly, glutathione *S*-transferase (GST) amounts of wild-type and Au_8-pX–treated YG8sR mice were significantly higher compared to YG8sR mice in cerebellum ($P < 0.0001$ and $P = 0.0001$), QA ($P < 0.0001$ and $P < 0.0009$), and TA ($P = 0.0009$ and $P = 0.0246$) (fig. S7C). A significant oxidized glutathione decrease in CNS and muscles of Au_8-pX–treated mice also suggested an improved detoxifying activity comparable to the basal wild-type conditions (cortex: $P < 0.0001$ versus YG8sR; cerebellum: $P = 0.0009$ versus YG8sR; QA: $P = 0.0002$ versus YG8sR; SL: $P = 0.0010$ versus YG8sR) (fig. S7C). Because Nrf2 is a transcriptional inducer of SOD, a key enzyme in preventing ROS increase (*47*), we measured the activity of SOD1 and SOD2 in Au_8-pX–treated and untreated tissues (fig. S7D). Whereas cytosolic SOD1 amount remained unchanged, we observed an increased activity of mitochondrial SOD2 (cortex and cerebellum: $P < 0.0001$ for Au_8-pX–treated YG8sR versus YG8sR; QA: $P = 0.0170$ for Au_8-pX–treated YG8sR versus YG8sR; SL: $P = 0.0495$ for Au_8-pX–treated YG8sR versus YG8sR) (fig. S7D).

Au_8-pXs affected mitochondria oxidative energy metabolism, as confirmed by the high content of mitochondrial ATP and the efficiency of ETC. Au_8-pX treatment induced improvement of ATP compared to untreated YG8sR mice in heart ($P = 0.0002$) and cortex ($P = 0.0114$), showing concentration values comparable to wild-type tissues (fig. S7E). Moreover, compared to YG8sR mice, Au_8-pX–treated mice showed that mitochondrial ATP increased in TA ($P = 0.0294$) and SL ($P = 0.0032$). Rescue of ETC functionality was found in cerebellum ($P = 0.0063$), heart ($P < 0.0001$), TA ($P = 0.0409$), and SL ($P = 0.0311$) of Au_8-pX–treated YG8sR mice compared to YG8sR (fig. S7E). Overall, these data showed that injection of Au_8-pXs ameliorates the pathology of frataxin loss in YG8sR mice by reducing oxidative damage and improving mitochondrial function in CNS and muscle tissues, consistent with neuromotor and cardiac functional improvement.

DISCUSSION

Although no effective treatment for FRDA exists, multiple therapies are being developed to increase frataxin, such as protein and gene replacement therapies, antioxidants, iron chelators, low oxygen, and HDACis (*13*, *31*, *15*). Here, we demonstrated that Au_8-pXs have broad catalytic effects against singlet oxygen, superoxide, and hydrogen peroxide. Moreover, single-dose systemic injection of Au_8-pXs into aged YG8sR mice ameliorates the FRDA pathology, including neurobehavioral deficits, muscle endurance, and heart contractile dysfunctions, suggesting therefore a potential therapeutical candidate to counteract the distinct mechanisms involved in FRDA.

The key advantage of this treatment is the capacity of the Au_8-pXs to migrate across the vessels and BBB and remain for prolonged time in several tissues including muscles, heart, and cerebellum of YG8sR mouse. Histopathological and motor-functional results indicate that Au_8-pX treatment is capable of blunting the oxidative stress of YG8sR mice and buffering intramitochondrial ROS by increasing SOD2 activity. This buffer activity prevents the oxidative damage on total DNA and membrane, allowing a higher efficacy of ETC and synthesis of ATP. Moreover, the buffered mitochondrial ROS allows to spare GSH for detoxification reactions, as demonstrated by the increased activity of GST, enhancing the protection from endogenous or exogenous oxidative stresses. This condition results into lower oxidative damages in whole cell membranes and nuclear DNA, two

components only indirectly touched by the oxidative mitochondrial damage induced by FXN deficiency. These results are in line with our previous data reporting the ability of Au_8-pXs to scavenge ROS (*16*). Thus, compared to other antioxidants treatments that specifically target mitochondria or cell membranes, the Au_8-pXs seem to act as multitarget protective agents in both FRDA cells and YG8sR mouse.

We showed that autophagy could have a relevant pathogenic role in FRDA cell and YG8sR animal model and that Au_8-pX treatment promoted the recovery of autophagy flux. These data may support that the excessive production of ROS in FRDA models could increase cell damage, whereas the role of autophagy could exhibit duality. Initiated autophagy by oxidative stress could clear mitochondria and proteins damaged by ROS, and in turn, it may contribute to reduce amounts of ROS by different pathways, such as p62 delivery and mitophagy. In addition, increasing evidence supports the notion that autophagy is critical for the survival or death of cells, suggesting a double-edged sword (*48*). YG8sR muscles showed a tubular pattern that indicates fusion activity of the mitochondrial network. However, we found in $BMSCs^{FRDA}$ cells the induction of mitochondrial MFN1 protein associated with high OXPHOS activity and an increase in MMP. This response of mitochondrial physiology may result from the mitochondrial network effort to buffer respiratory defects and oxidative stress (*49*). In addition, through induction or inhibition of autophagy of $BMSC^{FRDA}$, we confirmed the impairment of autophagy flux observed in $BMSC^{FRDA}$ basal conditions. Injection of Au_8-pXs resulted in LC3II/LC3I decrease and p62 increase in $BMSCs^{FRDA}$ and YG8sR mice, suggesting the recovery of the autophagic flux (*50*).

We also found increased Nrf2 expression in Au_8-pX–treated $BMSCs^{FRDA\#1}$ and in cerebellum of Au_8-pX–treated YG8sR mouse. The cytoprotective Nrf2 signaling has been shown to cooperatively interact with core autophagy proteins and, in particular, with p62 through the bond with ARE located in the p62 promoter (*51*). Hence, impaired autophagy could be crucial in modulating Nrf2 turnover and activity and ROS response efficiency (*52*). These findings suggest that maintenance of a functional feedback loop between antioxidant and autophagic responses may counterweight the issues of dysregulated cell homeostasis and mitigate FRDA progressive degeneration.

In line, we found that $BMSCs^{FRDA}$ mirror the harsh ROS-enriched environment of FRDA pathology and showed impaired Nrf2 activation and reduced p62, further increasing oxidative stress. Moreover, elevated oxidative stress in $BMSCs^{FRDA}$ builds a robust antioxidant defense by increasing NFS1 that may protect iron-sulfur clusters (*53*). NFS1 decrease and Nrf2 increase were associated to increased expression of mature frataxin mFXN in Au_8-pX–treated $BMSCs^{FRDA\#1}$ and cerebellum of Au_8-pX–treated YG8sR mouse, which may potentiate the antioxidant responses of Au_8-pXs. In Au_8-pX–treated cerebellum tissue, there was also an increase of PGC-1α and decrease of PPARγ protein expression. In contrast, the recovery of the autophagic flux in Au_8-pX–treated heart and QA muscle tissues was not accompanied by increased mFXN, and the NFS1, PGC-1α, and PPARγ were decreased. One possible explanation for such a difference is the diverse regulation of frataxin and autophagy-mediated signaling pathway in different cell types and tissues (*54*, *55*). Reasonably, because these differences are laid before the treatment, they may affect the degree of benefit exerted by Au_8-pXs and their scavenger activity. In addition, mitochondrial OXPHOS and aerobic metabolism are prevalent in cardiac tissues (*56*), whereas skeletal muscles favor oxidative or glycolysis metabolism depending on the muscle fiber composition (*57*). It is therefore likely that bioenergetic impairment caused by frataxin deficiency has ab initio a severe impact on the metabolism of the heart rather than skeletal muscle (*8*). However, it is noteworthy that we found the better response to Au_8–pXs in cerebellar granule neurons that are highly sensitive to the oxidative insults and represent a specific cellular target of the neurodegenerative process that evolves over time in YG8sR mice.

The major limitation of our approach was related to the unmodified insulin and glucose sensitivity in Au_8–pXs treated mice, likely because YG8sR mice may not represent the appropriate FRDA mouse model to test amelioration of diabetes. Further studies in different FRDA models will clarify the role of Au_8-pXs in pancreatic islet survival and glucose homeostasis. Overall, our data indicate a pleiotropic effect of Au_8-pX treatment based on the reduction of the oxidative damage coupled with the recovery of mitochondrial energetic metabolism and autophagy flux leading to an improvement of the motor and heart functions of YG8sR. From a therapeutic perspective, it is reasonable to suggest that a single infusion of Au_8-pXs may represent a promising approach for nongenetic treatment of FRDA.

MATERIALS AND METHODS

Study design

The primary aim of this study was to transfer the ROS scavenger activity of catalyst gold cluster superstructures Au_8-pXs into FRDA pathology, whose degenerative phenotype is linked to oxidative stress–activated signaling. In vitro, we used BMSCs derived from patients with FRDA and age-matched healthy donors to identify short-term Au_8-pX mechanisms of action, directly attributable to ROS buffering abilities. Considering that gold cluster superstructures did not act as sacrificial agents, we established the activation of a late/secondary response to Au_8-pX injection into the YG8sR model of FRDA. This effect was examined in murine tissues particularly affected by frataxin deficiency, such as CNS, peripheral nervous system, and heart, as well as in mildly damaged skeletal muscles and pancreas. Patients with FRDA (n = 2) and healthy donors (n = 2) were enrolled for bone marrow harvesting in the Unit of Neurology of the Fondazione IRCCS Ca' Granda Ospedale Maggiore Policlinico in Milan, Italy. All patients and YG8sR mice carry an intronic GAA triplet-repeat expansion in the first intron of the frataxin gene. Patients were homozygous for GAA expansion; the smaller GAA repeat sizes were 600 (patient 1) and 470 (patient 2), and the longer GAA expansion sizes were 730 (patient 1) and 1230 (patient 2). The study was approved by the Institutional Ethics Committee (2 April 2013, no. 792), and samples were collected with informed consent in accordance with the guidelines of the Committee on the Use of Human Subjects in Research of the Policlinico Hospital of Milan.

All the animal procedures were approved by the local Animal Ethics Committee of the Department of Molecular Biotechnology and Health Sciences of Turin and the Ministry of Health (PR 72833). Animals were maintained according to institutional animal welfare guidelines and legislation and under veterinary surveillance. The evaluation of Au_8-pX effects, in vitro and in vivo, has been performed by Western blot and immunostaining analyses. Experiments involving cell cultures were replicated independently at least three times per experiment, whereas experiments involving murine tissues were replicated independently at least twice. In vivo outcomes have been

further supported by reverse transcription quantitative polymerase chain reaction and biochemical analysis of Au_8-pX–mediated rescue from oxidative stress and damages associated to FRDA degeneration, as well as by skeletal and cardiac muscle function measurements. To verify the cluster circulation and the penetration into murine tissues, 12-month-old YG8sR mice ($n = 6$) were injected with 10 μM Au_8-pXs into the tail vein. Age-matched YG8sR mice ($n = 6$) were used as controls. Animals were euthanized after 30 days ($n = 3$ per experimental group) or 180 days ($n = 3$ per experimental group). For in vivo imaging, 12-month-old Au_8-pX–treated and untreated YG8sR mice ($n = 3$ mice per group) were used. For Au_8-pX treatment, 12-month-old animals were randomly assigned to experimental groups ($n = 10$ Au_8-pX YG8sR mice versus $n = 10$ YG8sR mice; $n = 6$ Au_8-pX C57Bl/6J mice versus $n = 6$ C57Bl/6J mice) on the day of injection. Histology score and motor behavior test were performed in a blind manner. Experiments were performed and analyzed with replicated and number of animals per group as indicated in the figure legends.

SUPPLEMENTARY MATERIALS

stm.sciencemag.org/cgi/content/full/13/607/eabe1633/DC1
Materials and Methods
Figs. S1 to S7
Tables S1 and S2
Data files S1 and S2
References (*58*, *59*)

View/request a protocol for this paper from *Bio-protocol*.

REFERENCES AND NOTES

1. V. Campuzano, L. Montermini, M. D. Molto, L. Pianese, M. Cossee, F. Cavalcanti, E. Monros, F. Rodius, F. Duclos, A. Monticelli, F. Zara, J. Canizares, H. Koutnikova, S. I. Bidichandani, C. Gellera, A. Brice, P. Trouillas, G. De Michele, A. Filla, R. De Frutos, F. Palau, P. I. Patel, S. Di Donato, J. L. Mandel, S. Cocozza, M. Koenig, M. Pandolfo, Friedreich's ataxia: Autosomal recessive disease caused by an intronic GAA triplet repeat expansion. *Science* **271**, 1423–1427 (1996).
2. R. Lill, Function and biogenesis of iron-sulphur proteins. *Nature* **460**, 831–838 (2009).
3. M. Ristow, M. F. Pfister, A. J. Yee, M. Schubert, L. Michael, C. Y. Zhang, K. Ueki, M. D. Michael II, B. B. Lowell, C. R. Kahn, Frataxin activates mitochondrial energy conversion and oxidative phosphorylation. *Proc. Natl. Acad. Sci. U.S.A.* **97**, 12239–12243 (2000).
4. S. Petrillo, E. Piermarini, A. Pastore, G. Vasco, T. Schirinzi, R. Carrozzo, E. Bertini, F. Piemonte, Nrf2-inducers counteract neurodegeneration in frataxin-silenced motor neurons: disclosing new therapeutic targets for Friedreich's ataxia. *Int. J. Mol. Sci.* **18**, 2173 (2017).
5. S. Sahdeo, B. D. Scott, M. Z. McMackin, M. Jasoliya, B. Brown, H. Wulff, S. L. Perlman, M. A. Pook, G. A. Cortopassi, Dyclonine rescues frataxin deficiency in animal models and buccal cells of patients with Friedreich's ataxia. *Hum. Mol. Genet.* **23**, 6848–6862 (2014).
6. M. J. Jasoliya, M. Z. McMackin, C. K. Henderson, S. L. Perlman, G. A. Cortopassi, Frataxin deficiency impairs mitochondrial biogenesis in cells, mice and humans. *Hum. Mol. Genet.* **26**, 2627–2633 (2017).
7. H. Lin, J. Magrane, A. Rattelle, A. Stepanova, A. Galkin, E. M. Clark, Y. N. Dong, S. M. Halawani, D. R. Lynch, Early cerebellar deficits in mitochondrial biogenesis and respiratory chain complexes in the KIKO mouse model of Friedreich ataxia. *Dis. Model. Mech.* **10**, 1343–1352 (2017).
8. H. Puccio, D. Simon, M. Cossee, P. Criqui-Filipe, F. Tiziano, J. Melki, C. Hindelang, R. Matyas, P. Rustin, M. Koenig, Mouse models for Friedreich ataxia exhibit cardiomyopathy, sensory nerve defect and Fe-S enzyme deficiency followed by intramitochondrial iron deposits. *Nat. Genet.* **27**, 181–186 (2001).
9. A. Bolinches-Amoros, B. Molla, D. Pla-Martin, F. Palau, P. Gonzalez-Cabo, Mitochondrial dysfunction induced by frataxin deficiency is associated with cellular senescence and abnormal calcium metabolism. *Front. Cell. Neurosci.* **8**, 124 (2014).
10. J. Woo, J. O. Min, D. S. Kang, Y. S. Kim, G. H. Jung, H. J. Park, S. Kim, H. An, J. Kwon, J. Kim, I. Shim, H. G. Kim, C. J. Lee, B. E. Yoon, Control of motor coordination by astrocytic tonic GABA release through modulation of excitation/inhibition balance in cerebellum. *Proc. Natl. Acad. Sci. U.S.A.* **115**, 5004–5009 (2018).
11. P. La Rosa, S. Petrillo, M. T. Fiorenza, E. S. Bertini, F. Piemonte, Ferroptosis in Friedreich's Ataxia: A metal-induced neurodegenerative disease. *Biomolecules* **10**, 1551 (2020).
12. A. Durr, M. Cossee, Y. Agid, V. Campuzano, C. Mignard, C. Penet, J. L. Mandel, A. Brice, M. Koenig, Clinical and genetic abnormalities in patients with Friedreich's ataxia. *N. Engl. J. Med.* **335**, 1169–1175 (1996).
13. A. Clay, P. Hearle, K. Schadt, D. R. Lynch, New developments in pharmacotherapy for Friedreich ataxia. *Expert Opin. Pharmacother.* **20**, 1855–1867 (2019).
14. S. Zhang, M. Napierala, J. S. Napierala, Therapeutic prospects for Friedreich's ataxia. *Trends Pharmacol. Sci.* **40**, 229–233 (2019).
15. G. Ocana-Santero, J. Diaz-Nido, S. Herranz-Martin, Future prospects of gene therapy for Friedreich's ataxia. *Int. J. Mol. Sci.* **22**, (2021).
16. B. Santiago-Gonzalez, A. Monguzzi, J. M. Azpiroz, M. Prato, S. Erratico, M. Campione, R. Lorenzi, J. Pedrini, C. Santambrogio, Y. Torrente, F. De Angelis, F. Meinardi, S. Brovelli, Permanent excimer superstructures by supramolecular networking of metal quantum clusters. *Science* **353**, 571–575 (2016).
17. B. Santiago-Gonzalez, A. Monguzzi, M. Caputo, C. Villa, M. Prato, C. Santambrogio, Y. Torrente, F. Meinardi, S. Brovelli, Metal nanoclusters with synergistically engineered optical and buffering activity of intracellular reactive oxygen species by compositional and supramolecular design. *Sci. Rep.* **7**, 5976 (2017).
18. Y. Gao, N. Shao, Y. Pei, Z. Chen, X. C. Zeng, Catalytic activities of subnanometer gold clusters (Au16–Au18, Au20, and Au27–Au35) for CO oxidation. *ACS Nano* **5**, 7818–7829 (2011).
19. S. Anjomani Virmouni, V. Ezzatizadeh, C. Sandi, M. Sandi, S. Al-Mahdawi, Y. Chutake, M. A. Pook, A novel GAA-repeat-expansion-based mouse model of Friedreich's ataxia. *Dis. Model. Mech.* **8**, 225–235 (2015).
20. S. Kim, M. Fujitsuka, T. Majima, Photochemistry of singlet oxygen sensor green. *J. Phys. Chem. B* **117**, 13985–13992 (2013).
21. M. C. DeRosa, R. J. Crutchley, Photosensitized singlet oxygen and its applications. *Coordin. Chem. Rev.* **233**, 351–371 (2002).
22. S. Goldstein, D. Aschengrau, Y. Diamant, J. Rabani, Photolysis of aqueous H2O2: quantum yield and applications for polychromatic UV actinometry in photoreactors. *Environ. Sci. Technol.* **41**, 7486–7490 (2007).
23. K. Akasaka, T. Suzuki, H. Ohrui, H. Meguro, Study on aromatic phosphines for novel fluorometry of hydroperoxides. 2. The determination of lipid hydroperoxides with diphenyl-1-pyrenylphosphine. *Anal. Lett.* **20**, 797–807 (1987).
24. A. Stepanova, J. Magrane, Mitochondrial dysfunction in neurons in Friedreich's ataxia. *Mol. Cell. Neurosci.* **102**, 103419 (2020).
25. M. Dominici, K. Le Blanc, I. Mueller, I. Slaper-Cortenbach, F. C. Marini, D. S. Krause, R. J. Deans, A. Keating, D. J. Prockop, E. M. Horwitz, Minimal criteria for defining multipotent mesenchymal stromal cells. The International Society for Cellular Therapy position statement. *Cytotherapy* **8**, 315–317 (2006).
26. N. Maio, A. Jain, T. A. Rouault, Mammalian iron-sulfur cluster biogenesis: Recent insights into the roles of frataxin, acyl carrier protein and ATPase-mediated transfer to recipient proteins. *Curr. Opin. Chem. Biol.* **55**, 34–44 (2020).
27. Y. Ikeda, S. Sciarretta, N. Nagarajan, S. Rubattu, M. Volpe, G. Frati, J. Sadoshima, New insights into the role of mitochondrial dynamics and autophagy during oxidative stress and aging in the heart. *Oxid. Med. Cell. Longev.* **2014**, 210934 (2014).
28. G. Twig, A. Elorza, A. J. Molina, H. Mohamed, J. D. Wikstrom, G. Walzer, L. Stiles, S. E. Haigh, S. Katz, G. Las, J. Alroy, M. Wu, B. F. Py, J. Yuan, J. T. Deeney, B. E. Corkey, O. S. Shirihai, Fission and selective fusion govern mitochondrial segregation and elimination by autophagy. *EMBO J.* **27**, 433–446 (2008).
29. M. Komatsu, H. Kurokawa, S. Waguri, K. Taguchi, A. Kobayashi, Y. Ichimura, Y. S. Sou, I. Ueno, A. Sakamoto, K. I. Tong, M. Kim, Y. Nishito, S. Iemura, T. Natsume, T. Ueno, E. Kominami, H. Motohashi, K. Tanaka, M. Yamamoto, The selective autophagy substrate p62 activates the stress responsive transcription factor Nrf2 through inactivation of Keap1. *Nat. Cell Biol.* **12**, 213–223 (2010).
30. H. Koutnikova, V. Campuzano, M. Koenig, Maturation of wild-type and mutated frataxin by the mitochondrial processing peptidase. *Hum. Mol. Genet.* **7**, 1485–1489 (1998).
31. X. Yao, X. Jing, J. Guo, K. Sun, Y. Deng, Y. Zhang, F. Guo, Y. Ye, Icariin protects bone marrow mesenchymal stem cells against iron overload induced dysfunction through mitochondrial fusion and fission, PI3K/AKT/mTOR and MAPK pathways. *Front. Pharmacol.* **10**, 163 (2019).
32. Y. Zhang, W. Zhai, M. Zhao, D. Li, X. Chai, X. Cao, J. Meng, J. Chen, X. Xiao, Q. Li, J. Mu, J. Shen, A. Meng, Effects of iron overload on the bone marrow microenvironment in mice. *PLOS ONE* **10**, e0120219 (2015).
33. B. D'Autreaux, M. B. Toledano, ROS as signalling molecules: mechanisms that generate specificity in ROS homeostasis. *Nat. Rev. Mol. Cell Biol.* **8**, 813–824 (2007).
34. N. Di Marzo, E. Chisci, R. Giovannoni, The role of hydrogen peroxide in redox-dependent signaling: Homeostatic and pathological responses in mammalian cells. *Cell* **7**, 156 (2018).
35. K. Chantrel-Groussard, V. Geromel, H. Puccio, M. Koenig, A. Munnich, A. Rotig, P. Rustin, Disabled early recruitment of antioxidant defenses in Friedreich's ataxia. *Hum. Mol. Genet.* **10**, 2061–2067 (2001).

36. R. Dey, K. Kemp, E. Gray, C. Rice, N. Scolding, A. Wilkins, Human mesenchymal stem cells increase anti-oxidant defences in cells derived from patients with Friedreich's ataxia. *Cerebellum* **11**, 861–871 (2012).
37. M. Reers, S. T. Smiley, C. Mottola-Hartshorn, A. Chen, M. Lin, L. B. Chen, [29] Mitochondrial membrane potential monitored by JC-1 dye. *Methods Enzymol.* **260**, 406–417 (1995).
38. D. V. Haute, J. M. Berlin, Challenges in realizing selectivity for nanoparticle biodistribution and clearance: lessons from gold nanoparticles. *Ther. Deliv.* **8**, 763–774 (2017).
39. L. Nogueira, I. Ramirez-Sanchez, G. A. Perkins, A. Murphy, P. R. Taub, G. Ceballos, F. J. Villarreal, M. C. Hogan, M. H. Malek, (–)-Epicatechin enhances fatigue resistance and oxidative capacity in mouse muscle. *J. Physiol.* **589**, 4615–4631 (2011).
40. K. Aquilano, S. Baldelli, B. Pagliei, M. R. Ciriolo, Extranuclear localization of SIRT1 and PGC-1α: an insight into possible roles in diseases associated with mitochondrial dysfunction. *Curr. Mol. Med.* **13**, 140–154 (2013).
41. G. K. Sakellariou, T. Pearson, A. P. Lightfoot, G. A. Nye, N. Wells, I. I. Giakoumaki II, A. Vasilaki, R. D. Griffiths, M. J. Jackson, A. McArdle, Mitochondrial ROS regulate oxidative damage and mitophagy but not age-related muscle fiber atrophy. *Sci. Rep.* **6**, 33944 (2016).
42. K. C. Kemp, A. J. Cook, J. Redondo, K. M. Kurian, N. J. Scolding, A. Wilkins, Purkinje cell injury, structural plasticity and fusion in patients with Friedreich's ataxia. *Acta Neuropathol. Commun.* **4**, 53 (2016).
43. M. Vreugdenhil, J. G. Jefferys, M. R. Celio, B. Schwaller, Parvalbumin-deficiency facilitates repetitive IPSCs and gamma oscillations in the hippocampus. *J. Neurophysiol.* **89**, 1414–1422 (2003).
44. B. Molla, F. Riveiro, A. Bolinches-Amoros, D. C. Munoz-Lasso, F. Palau, P. Gonzalez-Cabo, Two different pathogenic mechanisms, dying-back axonal neuropathy and pancreatic senescence, are present in the YG8R mouse model of Friedreich's ataxia. *Dis. Model. Mech.* **9**, 647–657 (2016).
45. M. Cnop, M. Igoillo-Esteve, M. Rai, A. Begu, Y. Serroukh, C. Depondt, A. E. Musuaya, I. Marhfour, L. Ladriere, X. Moles Lopez, D. Lefkaditis, F. Moore, J. P. Brion, J. M. Cooper, A. H. Schapira, A. Clark, A. H. Koeppen, P. Marchetti, M. Pandolfo, D. L. Eizirik, F. Fery, Central role and mechanisms of β-cell dysfunction and death in friedreich ataxia-associated diabetes. *Ann. Neurol.* **72**, 971–982 (2012).
46. Y. Shan, R. A. Schoenfeld, G. Hayashi, E. Napoli, T. Akiyama, M. Iodi Carstens, E. E. Carstens, M. A. Pook, G. A. Cortopassi, Frataxin deficiency leads to defects in expression of antioxidants and Nrf2 expression in dorsal root ganglia of the Friedreich's ataxia YG8R mouse model. *Antioxid. Redox Signal.* **19**, 1481–1493 (2013).
47. M. Zhang, C. An, Y. Gao, R. K. Leak, J. Chen, F. Zhang, Emerging roles of Nrf2 and phase II antioxidant enzymes in neuroprotection. *Prog. Neurobiol.* **100**, 30–47 (2013).
48. C. Evangelisti, C. Evangelisti, F. Chiarini, A. Lonetti, F. Buontempo, L. M. Neri, J. A. McCubrey, A. M. Martelli, Autophagy in acute leukemias: a double-edged sword with important therapeutic implications. *Biochim. Biophys. Acta* **1853**, 14–26 (2015).
49. H. Chen, J. M. McCaffery, D. C. Chan, Mitochondrial fusion protects against neurodegeneration in the cerebellum. *Cell* **130**, 548–562 (2007).
50. G. Kroemer, G. Marino, B. Levine, Autophagy and the integrated stress response. *Mol. Cell* **40**, 280–293 (2010).
51. M. Pajares, N. Jimenez-Moreno, A. J. Garcia-Yague, M. Escoll, M. L. de Ceballos, F. Van Leuven, A. Rabano, M. Yamamoto, A. I. Rojo, A. Cuadrado, Transcription factor NFE2L2/NRF2 is a regulator of macroautophagy genes. *Autophagy* **12**, 1902–1916 (2016).
52. A. T. Dinkova-Kostova, A. Y. Abramov, The emerging role of Nrf2 in mitochondrial function. *Free Radic. Biol. Med.* **88**, 179–188 (2015).
53. S. W. Alvarez, V. O. Sviderskiy, E. M. Terzi, T. Papagiannakopoulos, A. L. Moreira, S. Adams, D. M. Sabatini, K. Birsoy, R. Possemato, NFS1 undergoes positive selection in lung tumours and protects cells from ferroptosis. *Nature* **551**, 639–643 (2017).
54. N. Mizushima, M. Komatsu, Autophagy: Renovation of cells and tissues. *Cell* **147**, 728–741 (2011).
55. I. H. Harding, D. R. Lynch, A. H. Koeppen, M. Pandolfo, Central nervous system therapeutic targets in Friedreich ataxia. *Hum. Gene Ther.* **31**, 1226–1236 (2020).
56. T. Doenst, T. D. Nguyen, E. D. Abel, Cardiac metabolism in heart failure: Implications beyond ATP production. *Circ. Res.* **113**, 709–724 (2013).
57. M. Hargreaves, L. L. Spriet, Skeletal muscle energy metabolism during exercise. *Nat. Metab.* **2**, 817–828 (2020).
58. F. H. F. Lee, H. Zhang, A. Jiang, C. C. Zai, F. Liu, Specific alterations in astrocyte properties via the GluA2-GAPDH complex associated with multiple sclerosis. *Sci. Rep.* **8**, 12856 (2018).
59. G. Runwal, E. Stamatakou, F. H. Siddiqi, C. Puri, Y. Zhu, D. C. Rubinsztein, LC3-positive structures are prominent in autophagy-deficient cells. *Sci. Rep.* **9**, 10147 (2019).

Acknowledgments: We thank C. V. Pereira (Carlos T. Moraes Lab, University of Miami) for advice and help with Seahorse Oxygen flow and P. E. Porporato (MBC, Turin, Italy) for critical reading of the manuscript. **Funding:** This research was funded by Associazione "OGNI GIORNO"—per Emma—Onlus (Treviso, Italy), Associazione per il sorriso di Ilaria di Montebruno Onlus (Genova, Italy) (to Y.T.), and it presents independent research funded by Ricerca corrente FR230 Policlinico Hospital and Associazione Centro Dino Ferrari (to Y.T.). This work was also supported by Italian Ministry of Education, Universities and Research (MIUR), Ricerca Finalizzata 2016 ("Theory-enhancing") (to Y.T. and A.M.). Work at the University of Miami Miller School of Medicine was supported by the National Institute of Neurological Disorders and Stroke grant NINDS, 2R01NS079965-07 (to C.T.M.). Funders of the study had no role in the study design, data analysis, data interpretation, or writing of the report. **Author contributions:** C.V. and Y.T. conceived and designed all the experiments. C.V., Y.T., A.M., C.R., and G.R.M. wrote the paper. C.V., M.L., A.U., C.R., B.M., M.Boido., and M.Belicchi performed and acquired data from the in vitro experiments with BMSCs, as well as the characterization of wild-type and YG8sR mice injected or not with Au_8-pXs (functional measurements, animal tissue analysis, and characterization). R.J., C.L., and C.M. performed experiments of gold quantification. I.F., D.B., and R.R. performed the chemical analysis of Au_8-pX ROS scavenging ability in solution. C.V., M.P., and T.A., performed Seahorse analysis and ROS quantification in BMSCs and acquired data. G.F. and M.M. performed electronic microscopy. C.V., C.R., C.T.M., A.M., G.R.M., and Y.T interpreted and analyzed the data. All the authors stated were involved in the critical revision of the manuscript and approved the final version of the article, including the authorship list. The corresponding author had full access to all the data in the study and had final responsibility for the decision to submit for publication. **Competing interests:** C.V., A.M., and Y.T. are listed as inventors on a patent application (Nanocluster d'oro nel trattamento Atassia di Friedreich n. IT102019000020724) for Au_8-pX–mediated therapy for FRDA. M.L., A.U., C.R., R.J., B.M., M.Boido, M.Belicchi, C.M., C.L., I.F., D.B., M.P., T.A., R.R., C.T.M., and G.R.M. declare that they have no competing interests. **Data and materials availability:** All data associated with this study are present in the paper or the Supplementary Materials.

Submitted 4 August 2020
Accepted 15 June 2021
Published 18 August 2021
10.1126/scitranslmed.abe1633

Citation: C. Villa, M. Legato, A. Umbach, C. Riganti, R. Jones, B. Martini, M. Boido, C. Medana, I. Facchinetti, D. Barni, M. Pinto, T. Arguello, M. Belicchi, G. Fagiolari, C. Liaci, M. Moggio, R. Ruffo, C. T. Moraes, A. Monguzzi, G. R. Merlo, Y. Torrente, Treatment with ROS detoxifying gold quantum clusters alleviates the functional decline in a mouse model of Friedreich ataxia. *Sci. Transl. Med.* **13**, eabe1633 (2021).

Science Translational Medicine

Treatment with ROS detoxifying gold quantum clusters alleviates the functional decline in a mouse model of Friedreich ataxia

Chiara Villa, Mariella Legato, Alessandro Umbach, Chiara Riganti, Rebecca Jones, Beatrice Martini, Marina Boido, Claudio Medana, Irene Facchinetti, Dario Barni, Milena Pinto, Tania Arguello, Marzia Belicchi, Gigliola Fagiolari, Carla Liaci, Maurizio Moggio, Riccardo Ruffo, Carlos T. Moraes, Angelo Monguzzi, Giorgio R. Merlo and Yvan Torrente

Sci Transl Med **13**, eabe1633.
DOI: 10.1126/scitranslmed.abe1633

Friedreich ataxia golden age

Patients with Friedreich ataxia (FRDA) present neurological deficits and impaired muscle coordination. Mitochondrial energy conversion and oxidative phosphorylation have been shown to contribute to disease pathophysiology. Now, Villa *et al.* tested whether gold cluster superstructures (Au_8-pXs), previously shown to have antioxidant properties, could be effective in reducing the hallmarks of FRDA in vitro and in vivo. Au_8-pXs improved mitochondrial function, rescued autophagy flux, and increased FXN protein expression in mesenchymal stem cells from patients. In vivo, the treatment had therapeutic effects in a mouse mode, suggesting that Au_8-pXs might be effective in reducing FRDA symptoms.

Science Translational Medicine (ISSN 1946-6242) is published by the American Association for the Advancement of Science, 1200 New York Avenue NW, Washington, DC 20005. The title *Science Translational Medicine* is a registered trademark of AAAS.